Department of Physics and Astronomy
University of Heidelberg

Bachelor Thesis in Physics
submitted by

Frederik Leon Carstens

Born in Homburg (Germany)

2023

Magnetization Studies on the Correlated Electron Systems NdB_4, $MnTeMoO_6$ and $(Li_2Fe)SO$

This Bachelor Thesis was carried out by
Frederik Leon Carstens
at the
Kirchoff-Insitute für Physik at the Ruprecht-Karls-Universität Heidelberg
under the supervision of
Prof. Rüdiger Klingeler

Zusammenfassung

Magnetisierungsstudien an den drei korrelierten Elektronensystemen NdB_4, $MnTeMoO_6$ und $(Li_2Fe)SO$ mit Hilfe von SQUID-Magnetometrie sind Gegenstand dieser Arbeit. Isotherme feldabhängige Magnetisierungsmessungen am NdB_4 bei Temperaturen zwischen 9 K und 17.5 K mit Feldern parallel zur *c*-Achse ergänzen vorherige Untersuchungen und das resultierende magnetische Phasendiagram. Die Daten ermöglichen es, das Sättigungsverhalten in NdB_4 bei höheren Temperaturen zu verfolgen. Magnetisierungsmessungen an einer Dünnschichtprobe von $MnTeMoO_6$ ergaben aufgrund der geringen Probenmasse und des daraus resultierenden geringen magnetischen Signals nur unschlüssige Ergebnisse. Vorhergehende Berichte über Antiferromagnetismus konnten nicht bestätigt werden. Schließlich wurde polykristallines $(Li_2Fe)SO$, welches durch das mechanochemische Ball-milling-Verfahren hergestellt wurde, untersucht, um die Auswirkungen von thermischer Behandlung nach der Synthese zu verstehen. Das unbehandelte Material (LFRT) wurde zusammen mit Proben untersucht, die bei 300°C (LF300) bzw. 500°C (LF500) getempert wurden. Die Magnetisierungsstudien belegen irreversible Prozesse oberhalb von 320 K in der LFRT-Probe, was eine partielle Dekomposition impliziert. Signifikante ferromagnetische und superparamagnetische Beiträge zur Magnetisierung werden auf 3% enthaltenes elementares Eisen zurückgeführt. Diese Komponente nimmt mit der annealing-Temperature deutlich ab, in LF300 und LF500 wird klar weniger als 1% Eisen beobachtet. Die Daten liefern auch Beweise für das Vorhandensein von $Fe_{(1-x)}S$ mit x zwischen 0 und 0,06 in LFRT und LF300, was durch ferromagnetisches Verhalten unter 50 K und einen Sprung in der Magnetisierung bei 220 K angedeutet wird. Die Menge an $Fe_{(1-x)}S$ wird auf etwa 7% in LFRT und etwa 1,5% in LF300 geschätzt. Es wurde festgestellt, dass der Pauli-Paramagnetismus in $(Li_2Fe)SO$ unabhängig von der Annealing-Temperatur ist.

Abstract

Magnetization studies on the three correlated electron systems NdB_4, $MnTeMoO_6$ and $(Li_2Fe)SO$ by means of SQUID magnetometry are reported. Isothermal field dependent magnetization measurements on NdB_4 between 9 K and 17.5 K and fields parallel to the *c* axis complement previous studies and the resulting magnetic phase diagram. The data enable to trace a saturation in NdB_4 to higher temperatures. Magnetization measurements on a thin film sample of $MnTeMoO_6$ yielded only inconclusive results due to the small sample mass and resulting low magnetic signal. Previous reports of antiferromagnetism could not be confirmed. Lastly, polycrystalline $(Li_2Fe)SO$ produced through mechanochemical ball milling was investigated in order to clarify the effect of post-synthesis thermal treatment. The pristine material (LFRT) was studied alongside samples annealed at 300°C (LF300) and at 500°C (LF500) respectively. The magnetization studies evidences irreversible processes above 320 K in the LFRT sample which implies partial decomposition. Significant ferromagnetic and superparamagnetic contributions to the magnetization are attributed to 3% contained elementary iron. This component decreases signifi-

cantly with the annealing temperature and much less than 1% iron is observed in LF300 and LF500. The data also provide evidence for the presence of $Fe_{(1-x)}S$ with x between 0 and 0.06 in LFRT and LF300 as indicated by ferromagnetic like behavior below 50 K and a jump in magnetization at 220 K. The amount of $Fe_{(1-x)}S$ is estimated to be about 7% in LFRT and about 1.5% in LF300. Pauli-like paramagnetism in $(Li_2Fe)SO$ was found to be independent of the annealing temperature.

Inhaltsverzeichnis

1 Introduction **9**

2 Theoretical background **11**
2.1 Units in magnetism 11
2.2 Magnetic phenomena in solids 11
2.2.1 Diamagnetism 12
2.2.2 Paramagnetism 13
2.2.3 Magnetic anisotropy 13
2.2.4 Ferromagnetism 14
2.2.5 Antiferromagnetism 15
2.2.6 Magnetic frustration 16
2.2.7 Ferrimagnetism 17
2.2.8 Superparamagnetism 17
2.3 Introduction to compounds of interest 18
2.3.1 NdB_4 18
2.3.2 $MnTeMoO_6$ 18
2.3.3 $(Li_2Fe)SO$ 20

3 Experimental methods and procedure **21**
3.1 PPMS& MPMS3 21
3.2 SquidLab 23

4 Results of measurements and discussion **27**
4.1 Magnetization of single-crystalline NdB_4 27
4.2 Magnetization of single-crystalline $MnTeMoO_6$ 29
4.3 Magnetization of powdered $(Li_2Fe)SO$ 35

5 Conclusion and summary **51**

Kapitel 1

Introduction

> Thales too, as is related, seems to regard the soul as somehow producing motion, for he said that the stone has a soul since it moves iron.
>
> *Aristotle*[1]

The above quote talks about magnetite (Fe_3O_4), arguably one of the earliest magnetic materials known to man[2]. Magnetism is a phenomenon of contraries: It was discovered in ancient times and yet the underlying physics is not fully understood. Many magnetic phenomena are observed only in macroscopic systems while the fundamental interactions are inherently quantum mechanical: The electrons in atoms have a quantum mechanical spin and orbital angular momentum which causes a magnetic moment. In materials these moments interact strongly enough to overcome room temperatuer thermal fluctuations to cooperatively form ordered magnetic structures and introduce new facets to magnetism. This work presents studies of the magnetic properties in different materials. It will show the magnetization of a geometrically frustrated lattice in the form of NdB_4. Here a hypothesis on fractional magnetic plateaus at higher fields will be discussed and the obtained data will be used to extend a phase diagram of the material. Magnetism of a thin film $MnTeMoO_6$ was investigatedbut unfortunately the sample was too small for any significant signal. Lastly, different samples of the potential battery cathode material $(Li_2Fe)SO$ were magnetometrically investigated. The samples originate from batches which experienced differing annealing temperatures after synthesis, one sample was not heat treated. The samples thus contain impurities in different amounts. Using the obtained data, estimates on the contents of elementary iron and iron-sulfite (FeS) can be made. It is conjectured that $(Li_2Fe)SO$ is a Pauli paramagnet.

Kapitel 2

Theoretical background

2.1 Units in magnetism

Additionally to the SI-units, many contributions and devices in magnetic research use the cgs-system (centimeter-gram-second). The relevant units in cgs are:

Quantity	Symbol	cgs		SI
Energy	E	$1\,\mathrm{erg}$	$=$	$10^{-7}\,\mathrm{J}$
Magnetic flux density	B	$1\,\mathrm{G}$	$=$	$10^{-4}\,\mathrm{T}$
Magnetic field strength	H	$1\,\mathrm{Oe}$	$=$	$10^{3}/4\pi\,\mathrm{A/m}$
Magnetic moment	μ	$1\,\mathrm{erg/G}$	$=$	$10^{-3}\,\mathrm{J/T}$
Mass susceptibility	χ	$1\,\mathrm{erg/G/g}$	$=$	$(4\pi)^2 \times 10^{-10}\,\mathrm{Hm^2/kg}$
Molar susceptibility	χ	$1\,\mathrm{erg/G/mol}$	$=$	$(4\pi)^2 \times 10^{-13}\,\mathrm{Hm^2/mol}$

Tabelle 2.1: Units in magnetism for relevant quantities (according to [3]).

Another possible but not encouraged name for a quantity of 1 erg/G is 1 emu. The magnetization is also sometimes normalized to the number of magnetic ions and expressed in quantities of the Bohr magneton μ_B, which is then expressed in the unit μ_B/f.u. (formula unit).

2.2 Magnetic phenomena in solids

If a magnetic field is applied to a solid, it influences the individual atoms. The electrons in an atom each have a magnetic moment μ due to their spins and their orbital motion[4]. A magnetic moment in a magnetic field $\mathbf{H}$ results in an orientation-dependent energy

$$E = -\mu_0 \left(\mu \cdot \mathbf{H}\right) \tag{2.1}$$

with the magnetic permeability of vacuum μ_0. In a macroscopic system the magnetization $\mathbf{M}$ is defined[4] in order to describe the density of magnetic moments per volume V

$$\mathbf{M} = \frac{\mathrm{d}\mu}{\mathrm{d}V} \approx \frac{\overline{\mu}}{V}. \tag{2.2}$$

It edscribes the total magnetic state of a solid by averaging all its individual magnetic moments. To quantify the relationship between **M** and **H**, the magnetic susceptibility χ can be defined. It is generally a tensor quantity[5]

$$\chi_{ij} = \frac{\partial M_i}{\partial Hj}. \tag{2.3}$$

Measurements on single crystals will generally be conducted on a known and fixed axis so the anisotropy will be implied in the following text. If the relationship between magnetic field and magnetization is linear or approximately linear because the external field is small enough, χ can be simplified to be the quotient of the two quantities[6]

$$\chi = \frac{\partial M}{\partial H} \approx \frac{M}{H} \overset{\text{cgs}}{=} \frac{M}{B}. \tag{2.4}$$

The effect of the magnetization of a solid on the magnetic field is expressed by the relationship between magnetic field strength **H** and magnetic flux density **B** which is given by[5]

$$\mathbf{B} = \mu_0(\mathbf{H} + \mathbf{M}). \tag{2.5}$$

Most materials' magnetic behavior is governed by more than one behavior (see following subsections). It follows directly from the definitions of **M** and χ that the total susceptibility can be described as a linear superposition of the contributing phenomena's susceptibilities.

2.2.1 Diamagnetism

An external magnetic field will induce temporary magnetic dipoles in solids in order to minimize the energy contained in the field[6]. Following eq. (2.5), the resulting locally lowered field results in an antiparallel orientation of the magnetization and via the definition of the susceptibility (eq. (2.3)) a negative susceptibility. This diamagnetic (DM) tendency is present in all materials but rather weak and can be derived[6] to first order in perturbation theory as

$$\chi_{\text{DM}} = -n\frac{e^2\mu_0}{6m_\text{e}} Z_\text{eff} r^2[\text{SI}] = -n\frac{e^2}{6m_\text{e}c^2} Z_\text{eff} r^2[\text{cgs}] \tag{2.6}$$

with the particle density n, the electronic charge e, the number of electrons in the outermost shell of the atom Z_eff, the electronic mass m_e and the shell radius r. The diamagnetic contribution to the total magnetic susceptibility is rather weak and thus easily overshadowed by other phenomena. χ_{DM} is independent of the external magnetic field.

2.2.2 Paramagnetism

Paramagnetism (PM) describes the situation, where if in some atoms the spins of their electrons are unpaired, the spins or orbital moments are not compensated by other electrons. The resulting non-zero magnetic moment of the atom can align parallel to a magnetic field and lower the energy (eq. (2.1)) of the system[6]. This leads to a positive magnetization. The magnetization of an atom with total angular momentum quantum number $J = |\mathbf{S} + \mathbf{L}|$ has a characteristic dependence in $\mathbf{B}$ as it follows[6] the *Brillouin*-function $B_J(B)$:

$$\begin{aligned} M(B,T) &= n g_J \mu_\mathrm{B} J \left[\frac{2J+1}{2J} \coth\left(\frac{2J+1}{2J} y\right) - \frac{1}{2J} \coth\left(\frac{1}{2J} y\right) \right] \\ &=: M_\mathrm{sat}\, B_J(y) \qquad \left(y = \frac{g_J \mu_\mathrm{B} B}{k_\mathrm{B} T}\right) \\ &= M_\mathrm{sat} \frac{(J+1)}{3J} y + O(y^3) \end{aligned} \tag{2.7}$$

with Boltzmann's constant k_B, temperature T and Landé g factor g_J. The last line follows from a Taylor expansion of $B_J(y)$ in y. Figure 2.1 illustrates the Brillouin function $B_J(y)$ for various J. As can be seen, the magnetization will eventually saturate at M_sat for any J. The *Landé g-factor* describes the influences of orbit and spin momenta on the total angular momentum of the system. It is given as[6]

$$g_J = \frac{3}{2} + \frac{S(S+1) - L(L+1)}{2J(J+1)}. \tag{2.8}$$

In the case of free, isolated spins and sufficiently small magnetic fields, it can be derived[6] that the magnetic susceptibility is inversely proportional to the temperature T, which is called the *Curie law*:

$$\chi_\mathrm{PM} = \frac{C}{T} \propto T^{-1} \qquad \left(C = \mu_0 n \frac{\mu^2}{3 k_\mathrm{B}}\right). \tag{2.9}$$

The constant C is the Curie constant. Curie's law can be generalized to non-free spins by incorporating influences of molecular and crystal fields[5]. This is done by introducing the *Curie-Weiss temperature* θ_CW:

$$\chi_\mathrm{PM} = \frac{C}{T - \theta_\mathrm{CW}}. \tag{2.10}$$

This extension of Curie's law is named *Curie-Weiss law*. The general case of paramagnetism is described for the case of $\theta_\mathrm{CW} = 0$.

2.2.3 Magnetic anisotropy

If the crystal structure allows magnetically ordered states (as will be discussed in the following sections), the respective directions of ordering in the crystal will result

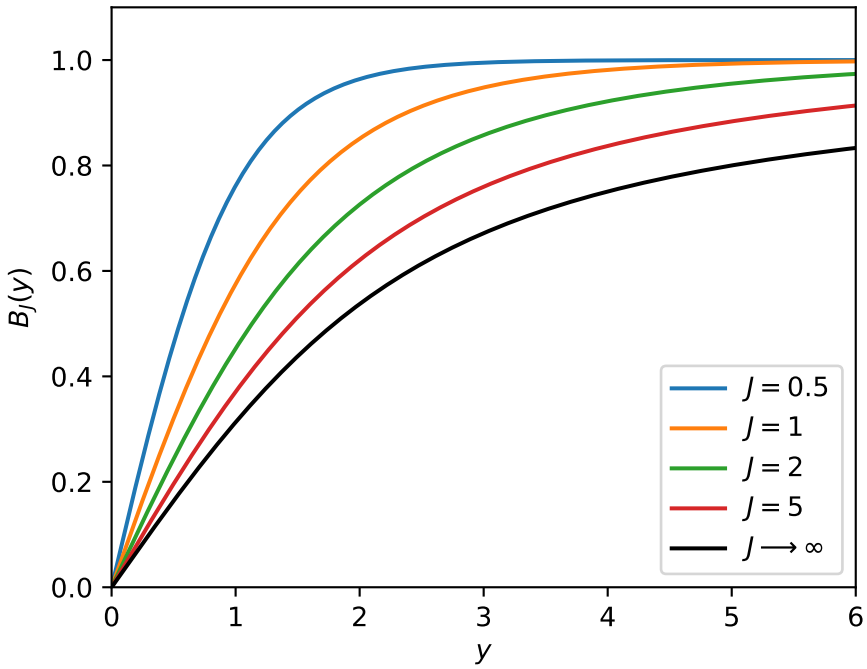


Abbildung 2.1: Brillouin function $B_J(y)$ plotted for different values of J.

in axes of easy and hard magnetizations[6]. Along these directions it is energetically favorable or unfavorable to have the magnetic moments lie. This *magneto-crystalline anisotropy* is caused by the local environment of the lattice[5]. *Shape anisotropy* is caused by the shape of the sample, which is relevant for objects with very different dimensions like thin films or needle shaped structures[5].

2.2.4 Ferromagnetism

Magnetic moments in a crystal interact with each other. If the interaction between neighbors favors a parallel orientation, the system as a whole may have a non-vanishing magnetization even without an external magnetic field[6]: This phenomenon is called Ferromagnetism (FM). A system has this property if the interaction energy of the spins' parallel orientation outweighs the entropy gain of other possible spin orientations[6]. For energetic reasons, the magnetic moments in a macroscopic ferromagnet will not all be parallel, but instead form magnetic domains of microscopic size[7]. Thermal fluctuations cause flipping of spins and thus may cause the destruction of such a spin structure. The critical temperature above which the long range order is destroyed, is the *Curie temperature* T_C.

Assuming the ferromagnet is in an initial state with zero net-magnetization and an

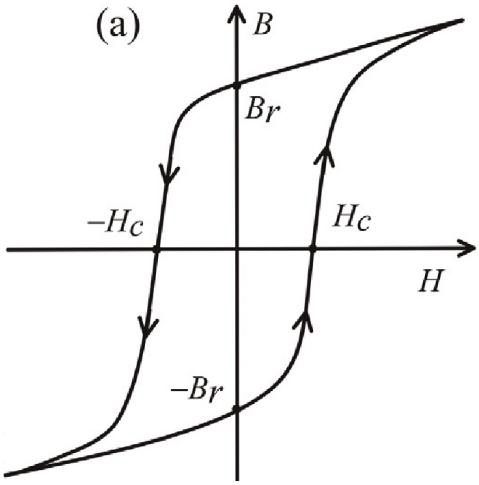


Abbildung 2.2: Idealized hysteresis loop of a ferromagnet, M_r, M_s and H_c are marked (taken from [8]).

external magnetic field is applied, its magnetization will rise and eventually saturate similar to that of of a paramagnet[6]. In contrast to a paramagnet however, the magnetization will not return to zero if the external field is completely removed, it will retain the *remanent magnetization* M_r. The domains are the cause for this hysteretic behavior as not all domains will return to their original fully disordered state when returning to a zero field leading to the remanent magnetization M_r.[7]. During the magnetization process the domains' walls will shift to allow for a more energetically favorable structure, at higher fields domains with an adverse orientation will flip and as a last step, all domains will rotate to be parallel to the applied field and overcome anisotropy. To achieve a vanishing magnetization, an adverse field - the *coercitive field* H_c - is required[6]. Lowering the field further leads to a magnetic saturation in the opposite direction and a consequent opposite remanence and coercitivity. This phenomenon is called *hysteresis* and is illustrated in a hysteresis loop, see figure 2.2.

It can be shown[6] that the susceptibility will follow the already mentioned Curie-Weiss law at $T \gg \theta_\mathrm{CW} = T_\mathrm{C}$

$$\chi_\mathrm{FM} \propto \frac{1}{T - T_\mathrm{C}}. \tag{2.11}$$

2.2.5 Antiferromagnetism

Some systems energetically favor an anti-parallel orientation of neighboring spins. Because the opposing magnetic moments cancel each other out, the lattice shows a macroscopic zero-field magnetization. The phenomenon is aptly called *antiferromagnetism*[4] (AFM). The microscopic structure can be illustrated as two shifted,

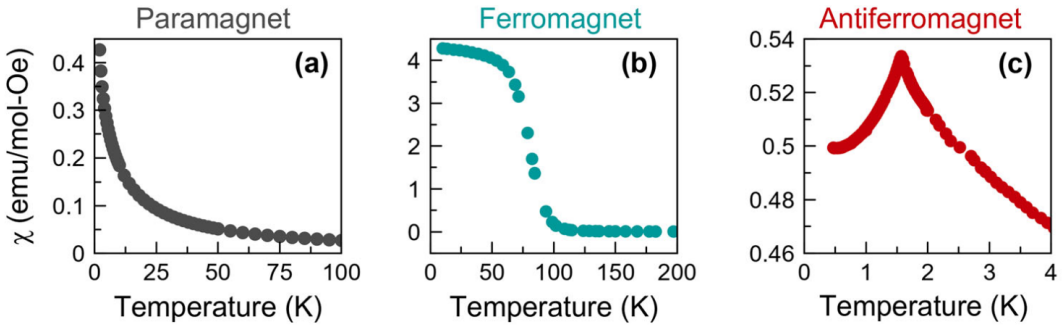


Abbildung 2.3: Exemplary temperature-dependence of the magnetic susceptibility χ for paramagnets, ferromagnets and antiferromagnets (taken from [9]).

half-filled ferromagnetic sublattices with opposite orientation[4]. Similar to ferromagnetism, this structure is only stable below a critical temperature, which is called the *Néel temperature* T_N. Antiferromagnets can be described by the Curie-Weiss law[6] for $T \gg \theta_\mathrm{CW} = -T_\mathrm{N}$

$$\chi_\mathrm{AFM} \propto \frac{1}{T + T_\mathrm{N}}. \tag{2.12}$$

The response of an antiferromagnetic structure to a magnetic field depends on the orientation of the field relative to the spins and on the anisotropy. In the case of a field perpendicular to the spins, these simply turn away from their original orientation towards the magnetic field until they reach saturation[6]. If the magnetic field is parallel to the spins, their exact behavior before saturation is dependent on the strength of the anisotropy. With a sufficiently weak anisotropy the moments perform a *spin-flop* at the magnetic field B_sf where they both turn to occupy an orientation, which has them partly perpendicular to the field similar to the previously described case and then align themselves towards the direction of the magnetic field[5]. Should the anisotropy be strong enough to not allow a spin flop, a *spin-flip* is possible: The orientation of the sublattice with magnetization opposite to the external field turns abruptly to the energetically favorable direction[5].

2.2.6 Magnetic frustration

In some AFM systems it is not possible that all interacting moments are antiparallel. This is for example the case in triangular lattices because at least two of the three spins (which all neighbor each other) on a triangle have to be parallel[6]. Other examples include Kagome-lattices in 2D[9] and tetragonal structures (e.g. spin ice) in 3D. Because the system cannot minimize the energy of all spin sites, the structure is called *frustrated*. A property of frustrated systems is a significant discrepancy between θ_CW and T_N because the frustration suppresses ordering[9]. To quantify the degree of frustration the quotient of Curie-Weiss temperature and Néel temperature

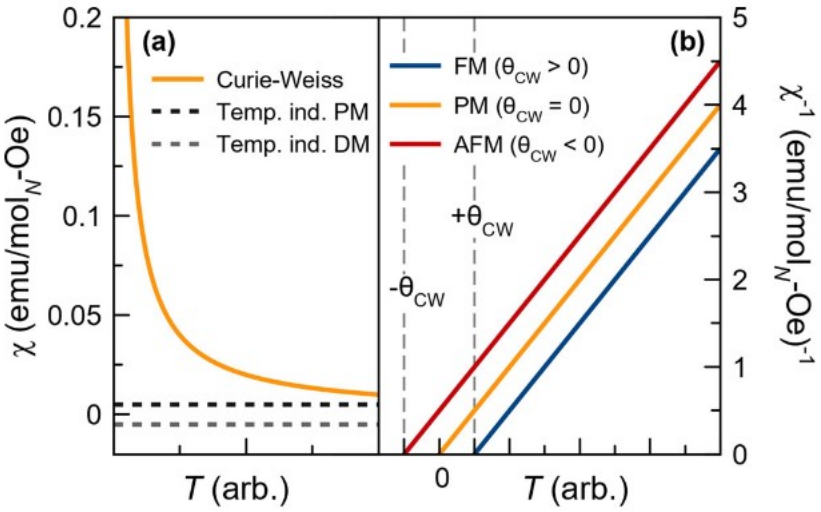


Abbildung 2.4: Illustration of the (a) magnetic susceptibility χ and (b) inverse magnetic susceptibility χ^{-1} according to the Curie-Weiss law (taken from [9]).

is used

$$f = \frac{\theta_{\mathrm{CW}}}{T_{\mathrm{N}}}. \tag{2.13}$$

2.2.7 Ferrimagnetism

Generalizing the image of the two sublattices in an antiferromagnet, it is not difficult to imagine that the two have different magnetizations. The resulting structure behaves macroscopically similar to a ferromagnet since it shows a hysteretic behavior albeit with a smaller saturation[9]. Similar to ferromagnetism, this phenomenon is called *ferrimagnetism* (FI). The general magnetic behavior of a ferrimagnet will also differ from a ferromagnet since the two sublattices will not necessarily behave in the same way at different temperatures resulting in a much more complex temperature dependence with multiple critical temperatures[9].

2.2.8 Superparamagnetism

A collection of sufficiently and not directly interacting small particles (nanoparticles) of a ferro- or ferrimagnetic material will show *superparamagnetic* behavior: Each particle is small enough to only consist of one domain[5]. If the temperature is above a size dependent *blocking temperature* T_B, the thermal fluctuations become large enough to overcome the anisotropy energy and continuously flip the domain's orientation along the magnetically easy axis. The magnetic nanoparticles (MNPs) do not form domains - the whole system behaves like a paramagnet above T_{B}[6] and is

called *superparamagnetic* (SPM). Below T_B the anisotropy energy is large enough to keep the orientation fixed of the particles fixed along one of the two possible axes.

2.3 Introduction to compounds of interest

2.3.1 NdB_4

NdB_4 is the first investigated compund. It is a metallic material[10] which is part of the family of rare earth tetraborides RB_4. The tetragonal crystal structure of NdB_4, space group $P4/mbm$[11], is illustrated in figure 2.5. B ions form octahedra which in turn are connected by one additional B ion and form rings in the ab plane. The Nd^{3+} ions, which are responsible for the magnetic behavior of the compound, occupy positions in a Shastry-Sutherland lattice (SSL), which is a geometrically frustrated structure[12], located in between the ring layers[13]. Interaction between the Nd^{3+} ions are antiferromagnetic[11] with the relevant interactions J_1 and J_2 marked by dashed and fully black lines in figure 2.5b. The two interactions are of different strength[11] but the exact values of J_1 and J_2 are not yet known.

Using Hund's rules, one can deduce that the three outer-shell electrons in the magnetic Nd^{3+} ions occupy states in a way which results in a total spin $S = \frac{3}{2}$ and orbital angular momentum $L = 6$. The total angular momentum is then $J = 9/2$.

Previous investigations[14,15] have found a phase transition from the paramagnetic state into an antiferromagnetic state at $T_N = 17.2$ K. This transition is reported to be characterized by a decrease in magnetic susceptibility in the ab plane while χ along the c axis does not behave anomalously at this temperature[14]. The provided explanation for this is a magnetic ordering in-plane at T_N while the out-of-plane ordering only occurs at lower temperatures[14]. The expectation of frustration is supported by experimental observations[11]. A phase diagram of NdB_4 along the c axis is depicted in figure 2.6.

2.3.2 $MnTeMoO_6$

The second compound analyzed in this work is $MnTeMoO_6$. It is part of the family of the additive tellurololybdates $MTeMoO_6$ (M = Mg, Mn, Co, Zn, Cd) and a semiconductor[16]. The compound crystallizes in the orthorhombic unit cells of the $P2_12_12$ space group which is shown in figure 2.7. In the crystal the Mn ions form a square lattice in the ab plane, these ions are part of MnO_6 octahedra. Between two of these layers, there is one layer comprised of MoO_4 tetrahedra and more complex TeO_4 polyhedra[17]. $MnTeMoO_6$ is a two-dimensional magnetic system[17]. Its magnetism is dominated by the Mn^{2+} ions[18].

It has been reported[17,18] that the magnetic ions are in a high-spin state and interact in an antiferromagnetic manner, they are oriented along the b axis (as marked in figure 2.7b). The Néel temperature was suggested to be $T_N = 58.8(6)$ K[17].

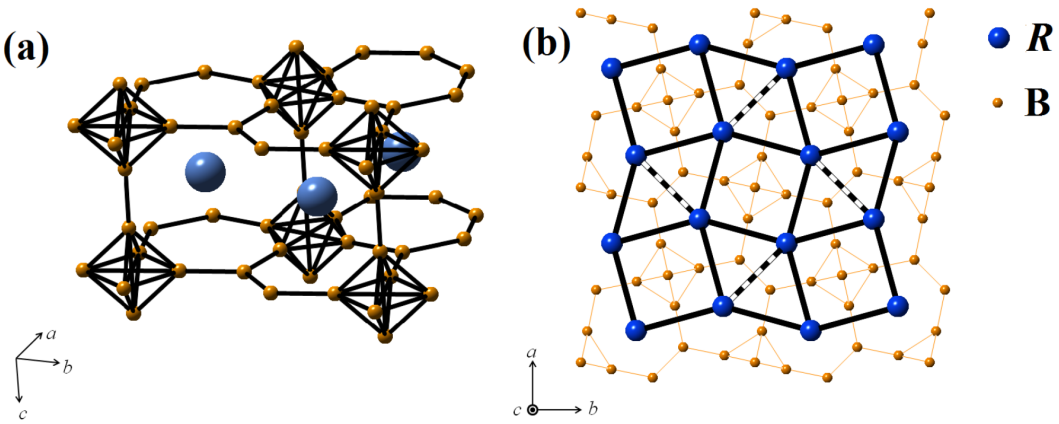


Abbildung 2.5: (a) Illustration of the crystal lattice of NdB_4 in 3D (b) planar view of the SSL lattice of the Nd ions (taken from [10]).

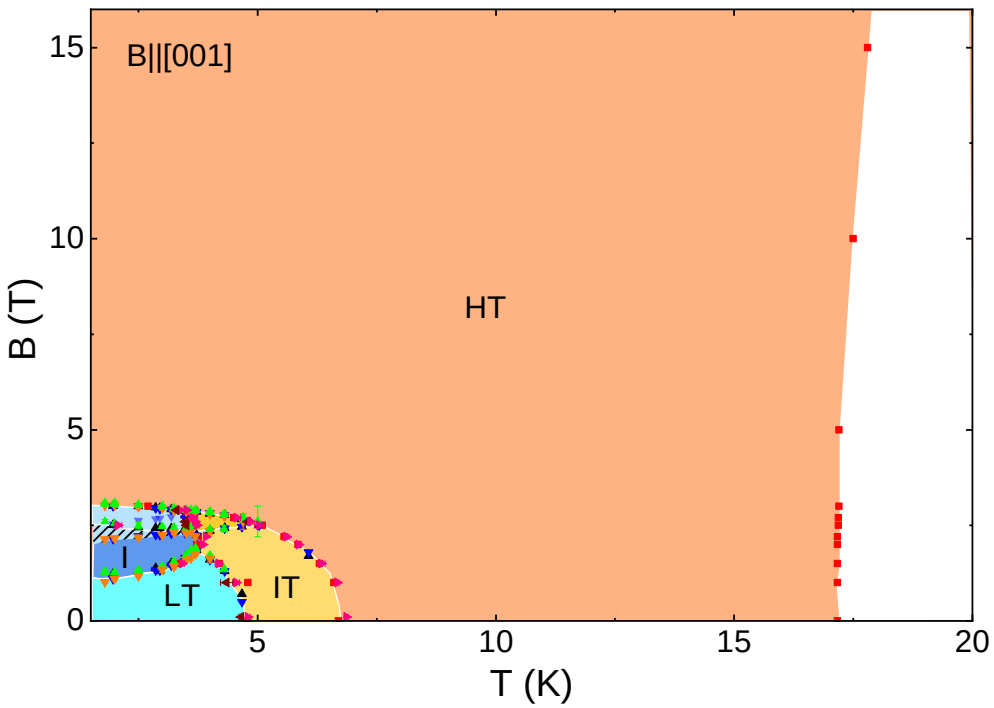


Abbildung 2.6: Phase diagram for NdB4 (Taken and adapted from [13]).

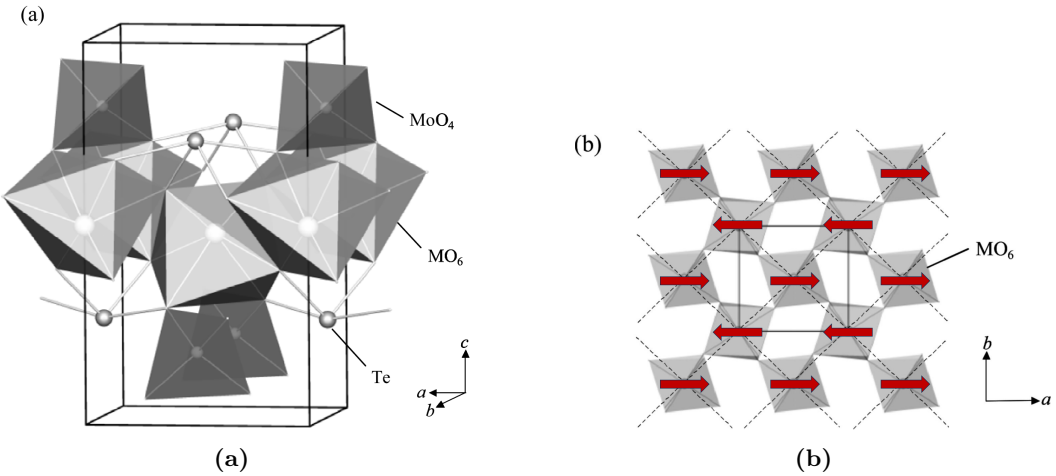


Abbildung 2.7: Visualizations of the crystal structure of $MnTeMoO_6$ (a) out of plane and (b) along the c axis with magnetic moments marked by red arrows. (taken and adapted from [17])

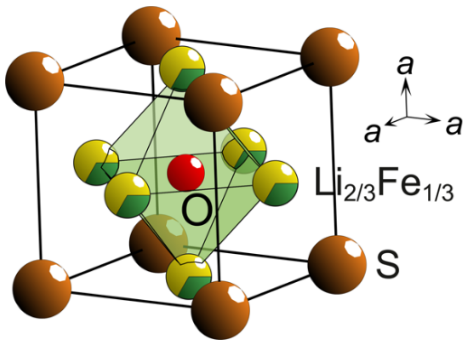


Abbildung 2.8: Crystal structure of $(Li_2Fe)SO$ (taken from [19]).

2.3.3 $(Li_2Fe)SO$

The last investigated material is $(Li_2Fe)SO$. The compound's structure is a cubic antiperovskite: the corners of the cube are occupied by S ions, the Li and Fe ions occupy the face-centered positions, finally the O ions sit in the center[19]. The atomic structure is depicted in figure 2.8. It has been shown[20] that the structure is intrinsically unstable. The only magnetic ions are the Fe^{2+} ions which are in a high-spin state ($S = 2$) and behave paramagnetically[19].

Kapitel 3

Experimental methods and procedure

3.1 PPMS& MPMS3

The magnetic measurements on the NdB_4 were performed using *Quantum Design*'s magnetometer PPMS®(**M**agnetic **P**roperties **M**easurement **S**ystem). It use a superconducting quantum interference device (SQUID) to reliably detect small changes in magnetic fields. For the other measurements on $MnTeMoO_6$ and $(Li_2Fe)SO$ the MPMS®3 (**P**hysical **P**roperties **M**easurement **S**ystem) also by *Quantum Design* was used. Both devices are located at the Kirchhoff-Institute for Physics (KIP) in Heidelberg. PPMS is a system capable of taking automated measurements of electric, magnetic, and thermal properties. The MPMS3 is a device designed for measuring magnetic and electric properties of samples similar to the PPMS. The dependencies studied directly with both systems are the isothermal magnetization as a function of the applied magnetic field $M(B)$ and the temperature dependent magnetization at constant field $M(T)$. During measurement the temperature and external field strength can be varied. The available temperature range is between 1.9 K and 400 K for the PPMS, and 1.8 K and 400 K for the MPMS3. Low temperatures are achieved using liquid helium cooling. The magnetic field is applied along a fixed axis inside the magnetometer and can be varied from -14 T up to 14 T in the PPMS, and between -7 T and 7 T in the MPMS3.

Samples to be measured with the MPMS or PPMS are inserted into sample holders (as depicted in figure 3.1). For all materials described in the following text, brass sample holders were used, which are made of a brass tube with an approximate length of 15 cm and a diameter of 3-4 mm. Bulk samples are clamped between two quartz crystals and additionally fixated with vacuum grease. Powder samples are contained in a gel capsule with a diameter of 3-4 mm which allows it to be placed directly into the sample holder. A brass sample holder containing a sample and the quartz crystals is depicted in figure 3.1. Empty sample holders are shown in figure 3.2. After insertion into the magnetometer, the sample holder is moved through the magnetometer. Based on that data a dipole response function fit can be used to extrapolate the exact position of the sample. Measurements in both devices follow the same basic measurement principle[22]: The sample is moved through the superconducting

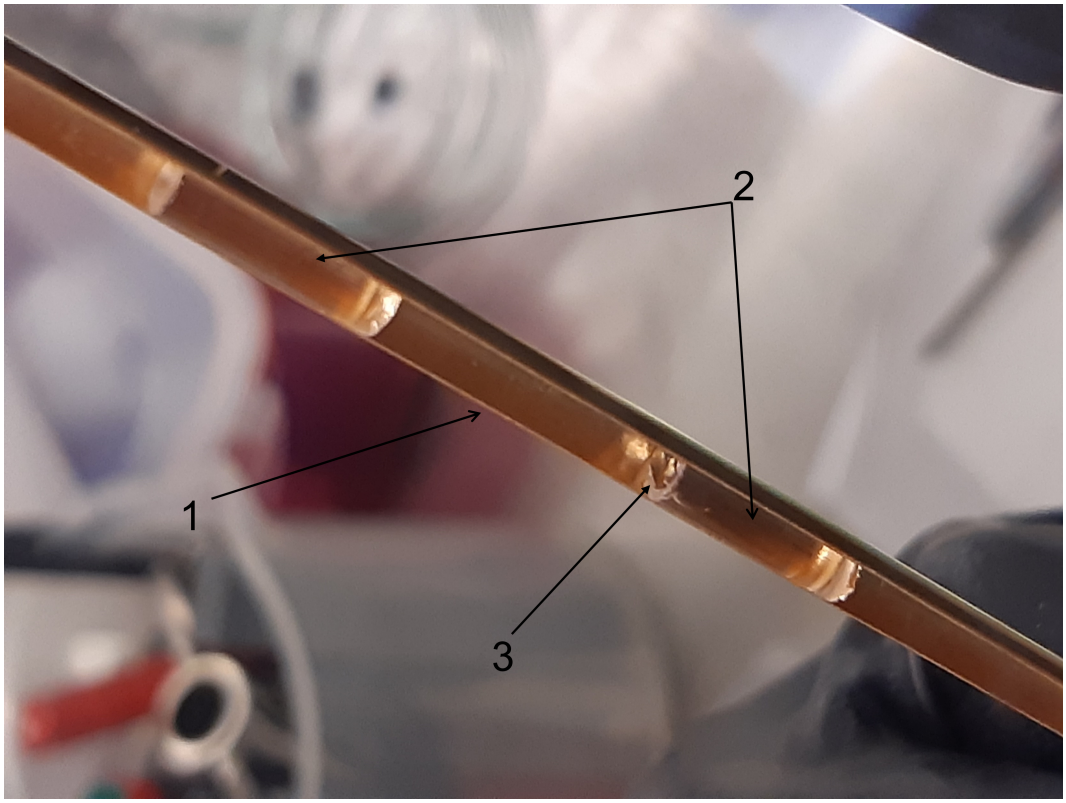


Abbildung 3.1: Brass sample holder (1) for MPMS and PPMS. The quartz clamps (2) are visible. Additionally, a sample can be seen mounted on one of the crystals (3). Courtesy of E. Walendy [21])



Abbildung 3.2: Empty brass sample holders for MPMS and PPMS with and without quartz.

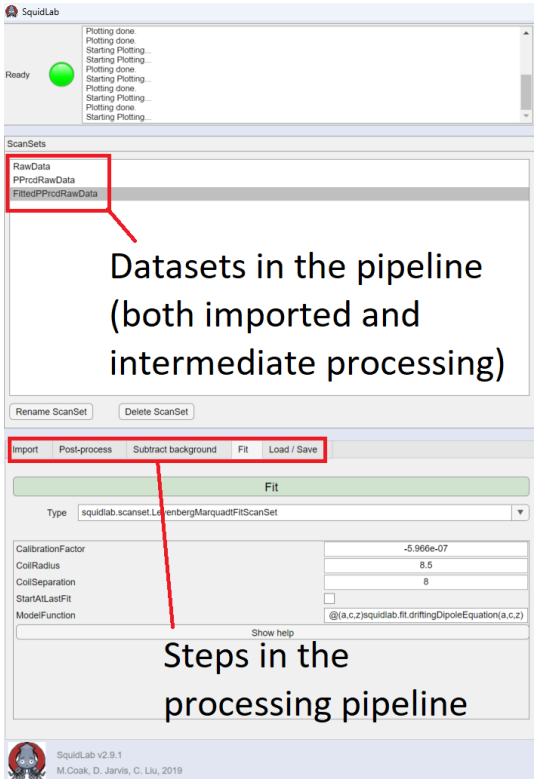
SQUID coil. Its magnetic moment will thereby cause a change in the magnetic field picked up as a signal by the coil and coupled into the sensitive SQUID. This signal is combined with the positions to determine the magnetic moment of the sample by fitting the response funciton into it. Because of the high sensitivity of the SQUID, the maximum possible resolution of the MPMS setup is 10^{-8} emu (source: *Quantum Design*). During the measurement the scans are saved to allow the option of manual fitting in case of problems with the data. All PPMS magnetometry measurements were executed in the VSM (Vibrating Sample Magnetometer) mode: The sample is being oscillated close to the coil with a variable frequency and amplitude. This allows for a resolution of 10^{-6} emu[23]. VSM is also available in the MPMS.

3.2 SquidLab

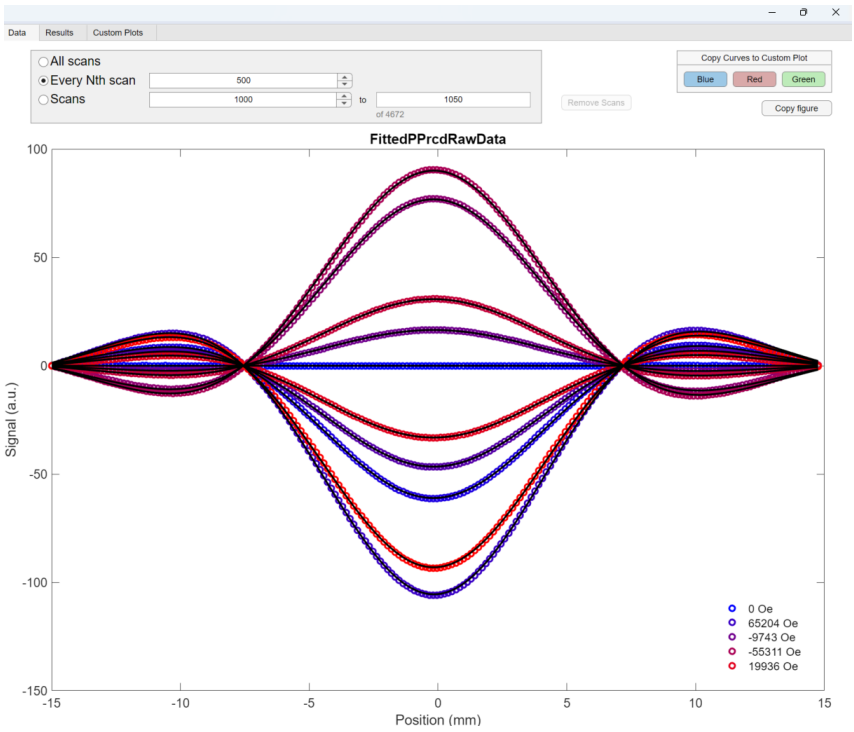
SquidLab[24] is a scientific program written for Matlab at the University of Warwick. It allows the user to manually process raw data obtained through various used magnetometers. This may be necessary if the detected signal is weak or more generally if the error needs to be further minimized from the device's internal routines. In the course of this work only the graphical user interface (GUI) was used although a command line interface is also available. The data processing is structured into a pipeline of steps:

- First the raw data needs to be imported into the program. A pre-configured import module for a number of magnetometers is available. Should background data be available, these can also be imported in the same manner.
- The post-processing stage offers several simple data manipulation tools: a moving average window smoothing (here, none will be performed), a drift subtraction, trimming and shifting. Subsequent scans may furthermore be averaged over; this is necessary if the background and measurement data measure at the same field/temperature but one of them performs more scans than the other at each setting.
- The background signal can be subtracted in the next step of the pipeline. This is performed either by linear interpolation of the necessary values in the background signal or by a assuming a dense enough dataset to take the nearest points. Usually the interpolation option is giving better results.
- A dipole function is fit into the resulting dataset. For this it is necessary to use the device's known parameters (here: CalibrationFactor=5.563*10^{-7}, CoilRadius=8.5, CoilSeparation=8, MultipoleOrder=4). Two fit options are offered. These are Levenberg-Marquard and SVD. The former is generally preferable as it is more apt at handling noise, SVD is recommended for smaller signals if the Levenberg-Marquard approach does not yield sufficient results.
- SquidLab offers the option to export the processed data as .txt files.

In between the data processing, the raw data is plotted in a separate window, specific scans (both from background as well as from the measured data) may be singled out and plotted in a second window. This is useful to compare background and measured signal, to find outliers or to check results of intermediary steps. Results of the fits are shown in another window as well. All graphics in SquidLab are plotted using Matlab and can thus be exported easily. Screenshots of SquidLab's GUI are shown in Figure 3.3.



(a)



(b)

Abbildung 3.3: Graphical User Interface of SquidLab with measured data (LF500). (a) shows the input fields for the data processing. (b) shows the data (blue/pink) with fitted curves (in black).

Kapitel 4

Results of measurements and discussion

4.1 Magnetization of single-crystalline NdB_4

The NdB_4 single crystal was investigated regarding its magnetization along the c axis. A photo of the single crystalline sample is shown in Figure 4.1. Its dimensions are 2 mm x 1.5 mm x 1 mm. The sample was weighed with a fine scale at KIP to have a mass of $m = 8.47(2)$ mg. The aim of the measurements is to provide more knowledge on the magnetic structure in response to applied magnetic fields along the c axis and extend the phase diagram as previously known and depicted in Figure 2.6.

The measurements performed in the course of this project investigate the isothermal magnetization behavior as a response to magnetic fields applied parallel to the c axis at temperatures chosen between 9 K and 17.5 K and fields up to 14 T. They are depicted in Figure 4.2 alongside results of previously performed studies at temperatures between 4 K and 7 K. Up to 3 T, the magnetization at 4 K is increasing without anomalies. A jump in M is clearly visible at 3 T in the 4 K magnetization data followed by a saturation like behavior up to highest measured fields. The jump like feature becomes much less pronounced and broadens in magnetic field with increasing temperature. For $T \geq 7$ K, the feature disappears and there is an almost linear slope in $M(B)$ followed by a saturation like behavior. Above 14 K this apparent saturation field can only be extrapolated because it is outside of the probed field range. The isothermal magnetizations at 17.2 K and 17.5 K do not differ significantly and are almost linear with only a very subtle curvature, which is expected because of small temperature difference. The observed plateau can be estimated to be $M_{\text{plateau}} = 1.8(3)\,\mu_{\text{B}}$/f.u.

A further approach to the analysis of the data lies in plotting the dynamic magnetic susceptibility $\chi = \partial M/\partial B$ (see eq. (2.4)). Results of this are depicted in Figure 4.3 for the data between 7 K and 17.5 K. The data for 7 K first show a linear growth up to 2.5 T followed by a broad kink and a similar decrease of $\partial M/\partial B$ up to 7 T. At higher temperatures (9 K and 14 K) the initial growth vanishes and is replaced by a constant value for χ between 0 T and 3 T and 4 T respectively. A similar but much less pronounced decrease is observed to 9.5 T and 11.5 T which ends in another constant regime. The data at 17.2 K and 17.5 K do not show the final constant

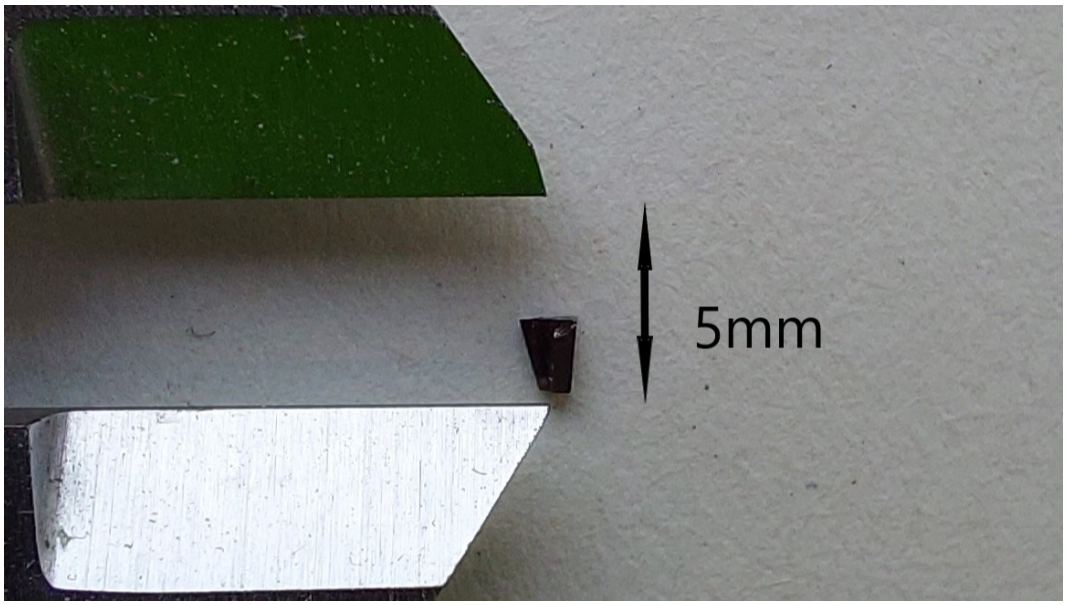


Abbildung 4.1: Photo of the NdB_4 sample.

regime anymore but show the same initial plateau followed by the dropping, which sets in at 5 T. Higher temperatures lead to a smoothing of the χ curves. In Figure 4.3 the transition between the initial plateau and the following drop are marked by red triangles, the constant magnetization at high B (where observed) is marked by a blue triangle.

The observed magnetization behavior is in agreement with previous investigations[25]. An explanation for the sudden increase in $M(B)$ could be either a spin flip/flop or another spin reordering phenomenon. This abrupt development within less than 0.5 T is however only observed for low temperatures $T \lesssim 6$ K; the smoother behavior observed in the other measurements stretches over much more than 1 T and has to be based in another mechanism. As seen in a previously constructed phase diagram Figure 2.6, the measurements which show a phase transition or at least a steep growth in M are all partially close to or in the intermediate temperature (IT) AFM phase. At higher temperatures, this is no longer the case and all the transitions are only the high temperature (HT) AFM phase. This means that the behavior can no longer be explained by a transition between previously reported phases. An explanation for the initial rise in $\partial M/\partial B$ could be that measuring at 7 K will be influenced by the IT phase and the phase transition between HT and IT at low fields. The drops at higher fields in the $\partial M/\partial B$ curves at 9 K and 14 K can be interpreted as the magnetization M entering the plateau. These features are added to the previously shown phase diagram for NdB_4, see Figure 4.4. The error is estimated from the determination of the fields (see Figure 4.3). It can be assumed from the position of the measured fields that the transition from the linear $M(B)$

into the plateau marks a defined region in the phase diagram. This region is marked in grey in Figure 4.4. Especially its bounds are still uncertain due to the difficulties in finding the higher critical fields from the field derivative of the magnetization (blue markers in Figure 4.3).

With the known angular momentum of the Nd^{3+} ions (see section 2.3.1), it is possible to get a naive estimate on the theoretically possible saturation magnetization of the material (see eq. (2.7)). Here the value of the g factor is $g_J = 8/11$ (eq. (2.8)) resulting in a theoretical saturation magnetization of $M_{\text{sat}}^{\text{th}} = 36/11 \approx 3.27\,\mu_{\text{B}}$/f.u. Previous investigations[13,25] on NdB_4 between 1.8 K and 7 K along the c axis have found similar plateaus with magnetization values of $M_{\text{plateau}} = 2.0(3)\,\mu_{\text{B}}$/f.u. at critical fields B_{plateau}. Values for B_{plateau} are 3 T for $T \leq 4$ K going up to 6 T for higher temperatures. So far, no further increase has been reported in fields up to $B||c = 50$ T (performed at 1.9 K[25]). A comparable behavior has also been observed in another rare earth tetraboride HoB_4[25]: The plateau for this material is similarly found at half of the theoretically possible saturation when applying fields larger than $B_{\text{plateau}}^{\text{HoB}_4} \approx 3$ T.

A possible explanation for this observation is given by Huo *et at.*[26]: They considered a general Shastry-Sutherland lattice with two additional interactions between lattice positions. It could be demonstrated via simulations that introducing an additional antiferromagnetic interaction J_3 between Nd ions, that do not already interact, and a ferromagnetic exchange J_4 between next nearest neighbors can cause the formation of a $M = 1/2M_{\text{sat}}^{\text{th}}$ plateau as depicted in Figure 4.5a. An illustration of the interactions in the geometry of the Shastry Sutherland lattice is given in Figure 4.5b. The underlying spin structure supporting this fractional saturation magnetization is predicted to be a ferrimagnetic configuration in the SSL. A ferro or ferrimagnetic structure would fit the observation of a saturation plateau. Anisotropy of the crystal is accounted for in the theoretical model, which results in the jumps to plateaus at B_{plateau} becoming less abrupt as reported experimentally[13,25]. A possible challenge to this explanation is that it has not yet been experimentally verified that the magnetization actually reaches $3.3\,\mu_{\text{B}}$/f.u. at any field strength. Therefore, it is not certain that the measured value really corresponds to the $1/2M_{\text{sat}}^{\text{th}}$ plateau. Observing a further increase in $M(B)$ at sufficiently high fields would be a piece of evidence for this explanation.

4.2 Magnetization of single-crystalline $MnTeMoO_6$

A thin film sample of $MnTeMoO_6$ was studied through magnetization measurements at the MPMS. The sample was weighed using a fine scale at KIP and had a mass of $m = 0.43(2)$ mg. Its surface sides are flat areas of dimensions 3×3 mm. Photos of the sample are depicted in Figure 4.6. The film has been oriented using Laue X-ray diffraction by L. Gries and T. Kleinbek, which confirmed that the ab plane coincides with the film plane. To extend the sparse previous knowledge on the magnetic be-

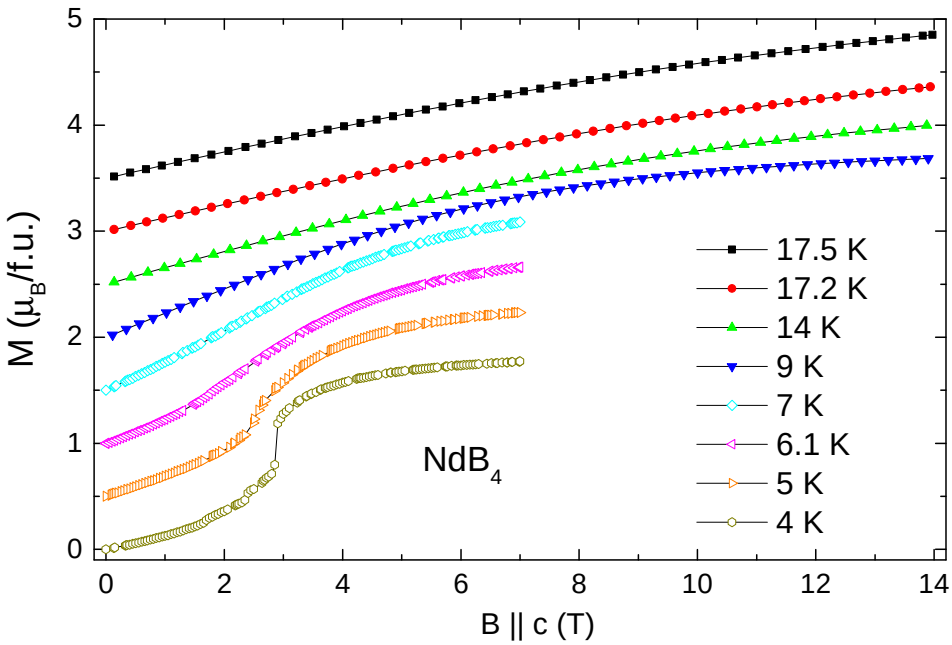


Abbildung 4.2: Isothermal field dependent magnetization $M(B)$ along the c axis on a NdB_4 single crystal. The curves are offset by $0.5\,\mu_B$/f.u. each. Data by S. Spachmann is plotted in empty dots.

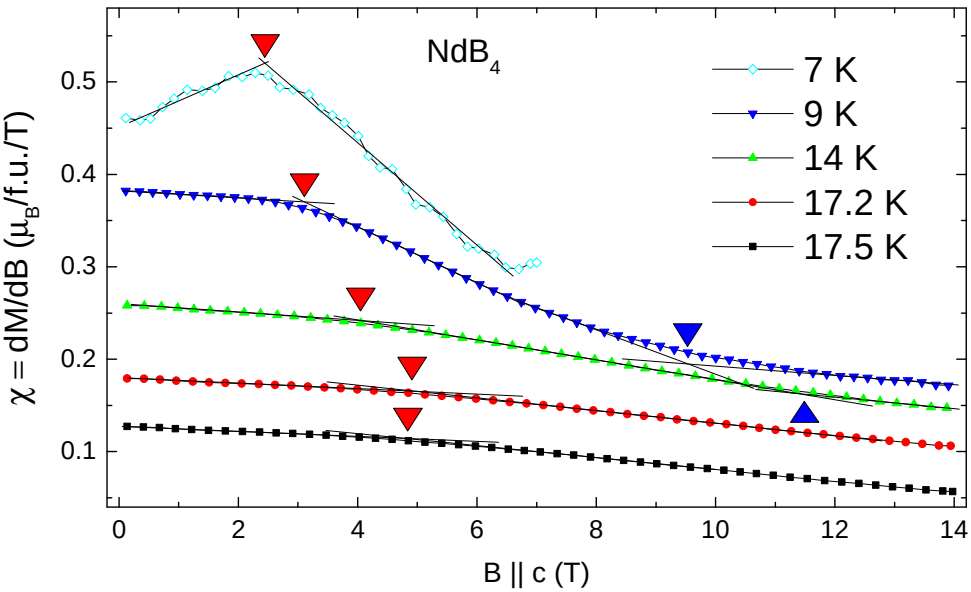


Abbildung 4.3: Dynamic magnetic susceptibility $\chi = \partial M/\partial B$ along the c axis from isothermal magnetization measurements on a NdB_4 single crystal. The curves are offset by $0.05\,\mu_B$/f.u./T each. Data by S. Spachmann is plotted in empty dots.

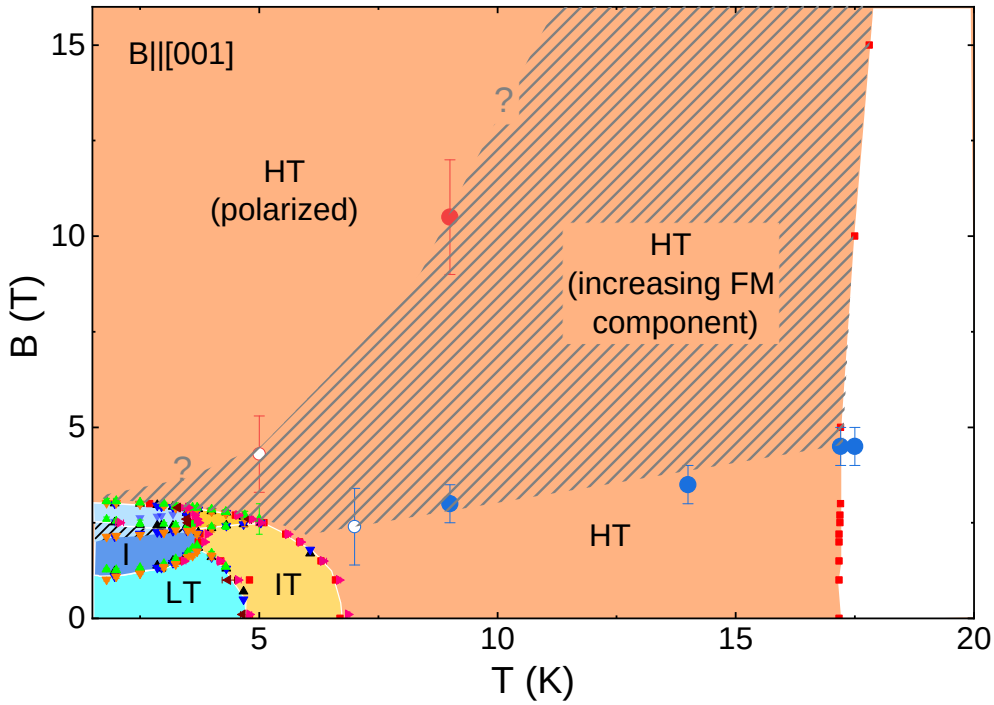
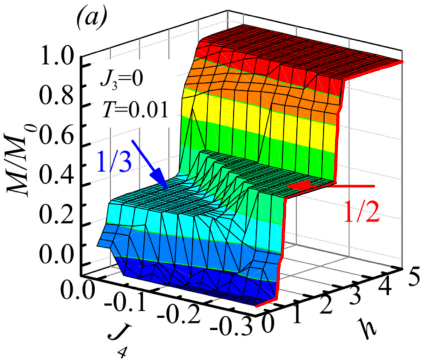
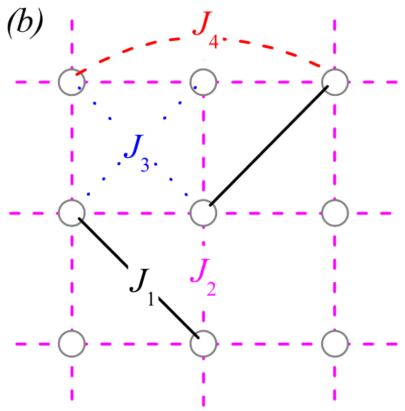


Abbildung 4.4: Phase diagram of NdB_4 for magnetic fields B along the c axis. HT, IT & LT denote antiferromagnetic phases: HT stands for high temperature, IT for intermediate temperature and LT for low temperature. The data points in blue and red on the edge of the FM phase are added from the new measurements, the hollow data points are from measurements undertaken by S. Spachmann. (Taken and adapted from [13]).



(a) Field dependent magnetization $M/M_0(h)$ as a function of additional ferromagnetic J_4. The edge colored in red marks a potential magnetization curve which displays the observed phenomenology (see text)



(b) S-S lattice including two additional interactions, J_3 is antiferromagnetic, J_4 is ferromagnetic.

Abbildung 4.5: Introducing additional antiferromagnetic and ferromagnetic interactions J_3 and J_4 into a S-S lattice leads to the formation of a plateau of half theoretical saturation magnetization (images taken and adapted from [26]).

havior of $MnTeMoO_6$ it is necessary to conduct more magnetization measurements on it.

During the measurements, a magnetic field $B||c$ was applied perpendicular to the ab plane. First the isothermal field dependent magnetization $M(B)$ was measured at temperatures of 1.8 K and 17 K, later 4 K and 10 K were also probed. Because of a problem with the measurement computer, raw data was only available for analysis from the latter two temperatures. For the earlier measurements only the already postprocessed data could be used, this cause have minor inaccuracies due to suboptimal fitting in the MPMS' internal data analysis programs. A second measurement was conducted to determine the temperature dependent magnetization with an applied field $M(T)$. To improve the quality of the results, the raw data was manually analyzed using the program *SquidLab*[24]. It allows for more oversight over the data processing pipeline and a separate background correction. Background data of the used sample holder at 1.8 K was previously measured by T. Kleinbek.

The $M(B)$ data is plotted in Figure 4.7. The data show a linear behavior. A gradient can be estimated for all temperatures, it is slightly higher for 1.8 K and 4 K at $\partial M/\partial B = 2.7(1) \times 10^{-2}\,\mathrm{erg/G^2/mol}$ then at 10 K and 14 K with $\partial M/\partial B = 2.6(1) \times 10^{-2}\,\mathrm{erg/G^2/mol}$. The inset of Figure 4.7 zooms in on the low B region. It can be seen that the data for 1.8 K and 17 K start out at slightly negative values, $|M| < 50$ erg/G/mol, while the behavior at 4 K and 10 K shows no such offset.

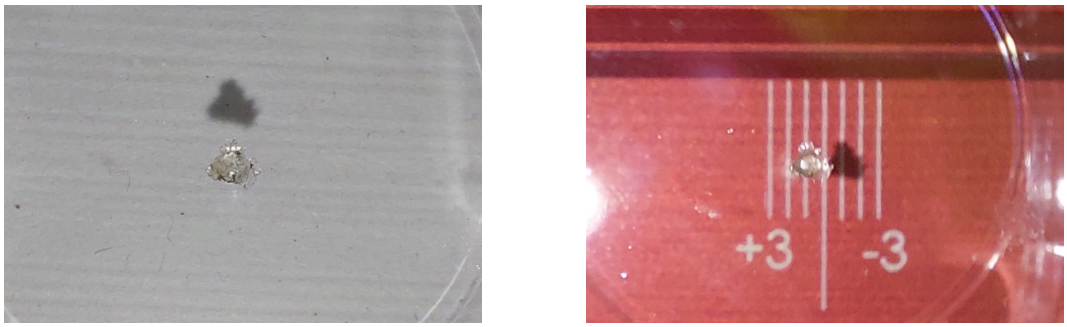
Since this small effect is not visible with the data processed in SquidLab, it stands to reason that this might be due to faulty extrapolation on the side of the MPMS and was corrected by the SquidLab analyis.

Results of the $M(T)$ measurements are depicted in Figure 4.8 in the form of the static magnetic susceptibility $\chi(T) = M(T)/H$. Alongside this, reference data from a bulk sample by Doi *et al.*[17] is plotted. The measured data show a slight decrease at $T \approx 10$ K coming from lowest temperatures followed by a near constant positive ergime of $\chi \approx 1.7(1) \times 10^{-2}$ erg/G/mol with only a slight growth towards higher temperatures. This is contrasted by the reference data which displays a significant maximum at $T = 33$ K, followed by a Curie Weiss like $1/T$ behavior for higher T[17]. Both datasets are on the same order of magnitude but the reference starts out at $\approx 3.2 \times 10^{-2}$ erg/G/mol and the maximum reaches $\approx 4.0 \times 10^{-2}$ erg/G^2/mol. The two curves intersect at $T \approx 210$ K.

The Mn^{2+} ions have a $S = 5/2, L = 0$ state which leads to $g_J = 2$ and an expected saturation magnetization of $M_{\text{sat}} = 5\,\mu_{\text{B}}$/f.u. ≈ 28000 erg/G/mol. Contrasting this with the measured slope in $M(B)$, a lower estimate can be made on the magnetic field necessary to bring the sample into saturation: If the growth continued further with the same slope, saturation would be reached at the saturation field $B_{\text{sat}} = M_{\text{sat}}/(M/B) = 165(9)$ T. Plugging the fields and the temperature into eq. (2.7) results in a maximum value for the parameter $y = \frac{g_J \mu_{\text{B}} B}{k_{\text{B}} T} = 5.2$. Comparing this to Figure 2.1, it becomes obvious that the observed behavior is problematic since the data has no visible curvature, which would be expected for such y.

Differences between the measured values and the reference data concerning the isothermal magnetization $M(T)$ are significant. The measured sample does not show the prominent features such as the maximum or the $1/T$ decrease. It should be noted that the sample used in the reference[17] is not a thin film but a pellet. The two samples should still exhibit analogous behavior because the magnetic moments lie along the b axis (see Figure 2.7b) which falls in the film plane. A temperature independent positive susceptibility can sometimes be explained as being either Pauli or Van Vleck paramagnetism. These two influences can however be ruled out in this case. Pauli paramagnetism requires the material to be metallic, which $MnTeMoO_6$ is not as explained in section 2.3.2. Van Vleck paramagnetism can be ruled out because this is typically only relevant for systems containing Eu^{3+}, Sm^{3+} or larger ions and is negligible otherwise.

The recorded signal is very weak because of the small amount of sample (0.43 mg corresponds to only 1.1×10^{-6} mol). A comparison of the signal with the background of the sample holder is depicted in Figure 4.9a (compared to a sample of $(Li_2Fe)SO$ as described in the following section), both are of similar strength. This implies that the part of the signal caused by the sample itself is significantly smaller than the background. An uncertainty in the sample holder's signal will dominate the results. The measured signal may be interpreted as an inverted (through subtraction from the vanishing signal of the sample) diamagnetic source which is the diamagnetic



(a) **(b)**

Abbildung 4.6: Photos of $MnTeMoO_6$ sample taken after the measurement.

brass sample holder. Since the only available background data for isothermal magnetization was taken at 1.8 K and not at the other measured temperatures, it had to be used to correct all measurements and thus introduced another source of uncertainty considering the relative magnitude of the signal in the $M(B)$ data. The background data in the $M(T)$ measurement and the $M(T)$ data were taken at the same field $B = 0.1\ T$, yet still show aforementioned discrepancy. Because of the mentioned factors it is likely that the observed magnetization does not show the behavior of $MnTeMoO_6$. An improved understanding could be achieved by using a larger sample and trying to get a stronger signal. It can also prove useful to exchange the brass holders with quartz ones as these cause a smaller magnetic signal[22].

4.3 Magnetization of powdered (Li_2Fe)SO

Three (Li_2Fe)SO samples were studied. All were produced through mechanochemical *ball milling*[27] synthesis at the Leibniz-Institut für Festkörper- und Werkstoffforschung Dresden (IFW). The differences between the samples are based in the heat treatment (annealing) after the ball milling:

- Sample LFRT was not heat-treated. It has a mass of $m = 16.4$ mg.
- Sample LF300 was heat-treated at 300°C following the ball milling. It has a mass of $m = 8.1$ mg.
- Sample LF500 was heat-treated at 500°C following the ball milling. It has a mass of $m = 11.7$ mg.

All samples were weighed by B. Dong. They consist of a powder of (Li_2Fe)SO with grains of sizes up to ca. 5 μm[27]. The crystallites' sizes are dependent on the heat treatment temperature, low temperature annealing results in generally smaller crystallites of less than 100 nm (60 nm at 300°C), higher temperatures lead to larger crystallites (110 nm at 500°C) as seen in Figure 4.11. An increase in heat-treatment temperature is reported to cause clumping together of the grains into larger clusters,

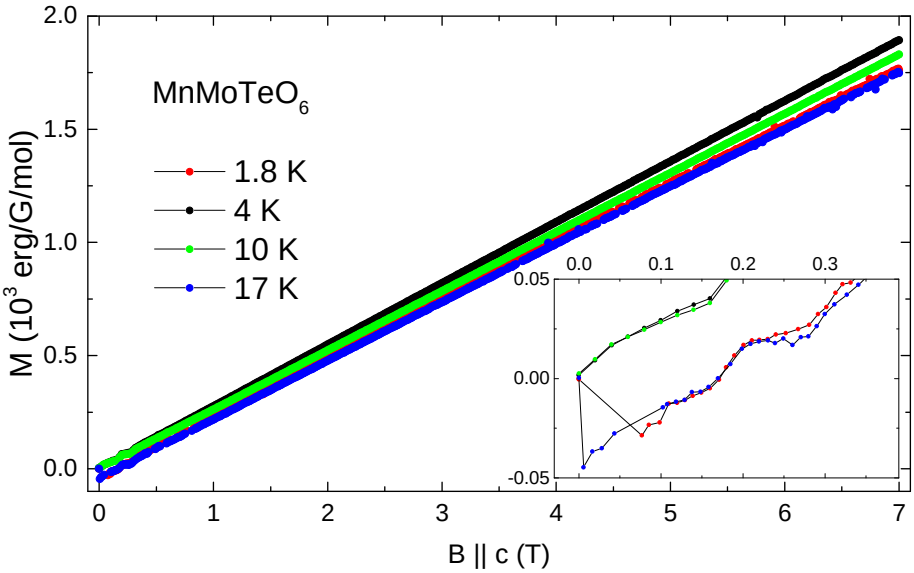


Abbildung 4.7: Measured isothermal magnetization along the c axis of $MnMoTeO_6$ as a function of parallel magnetic field at different temperatures. The inset is zoomed in on the low field region.

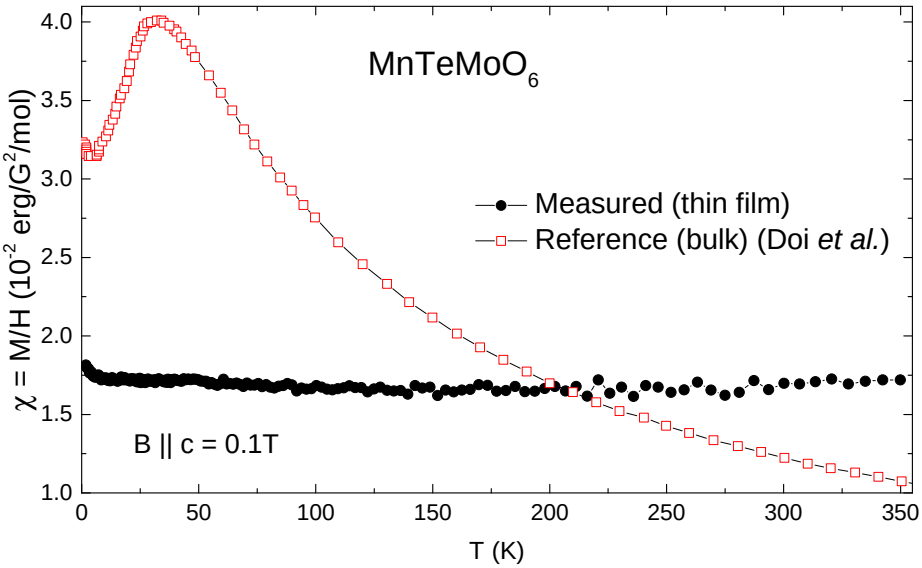
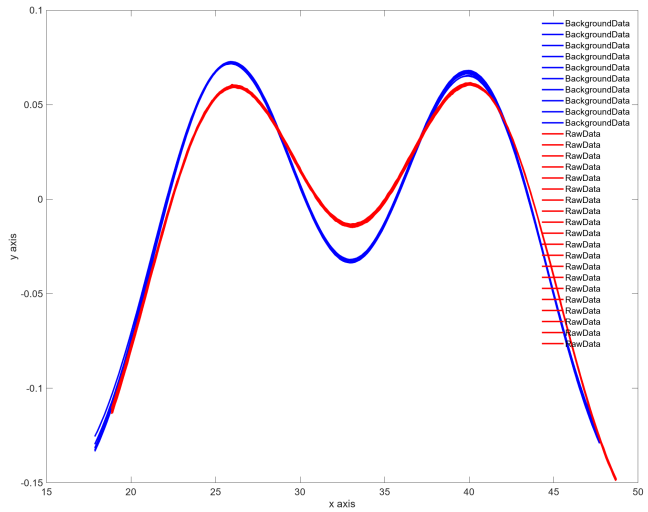
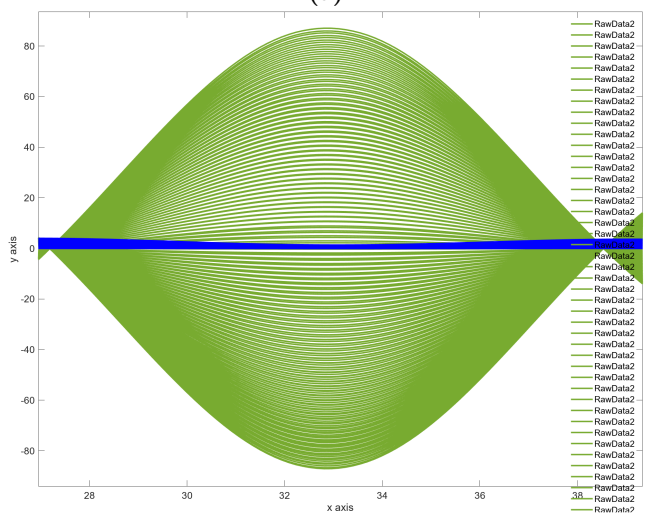


Abbildung 4.8: Measured magnetic susceptibility along the c axis of $MnMoTeO_6$ as a function of parallel magnetic field at different temperatures, results of [17] are added as a reference.



(a)



(b)

Abbildung 4.9: Comparing signal strengths of $MnTeMoO_6$ in red (a) and LF500 in green (b) with background (blue) graphed in SquidLab.

Sample	M_{sat}(erg/G/mol)		M_r(erg/G/mol)		$\chi_{PM}(10^{-3}\,erg/G^2/mol)$	
	1.8 K	300 K	1.8 K	300 K	1.8 K	300 K
LFRT	390(10)	350(6)	120(10)	60(5)	4.4(1)	3.6(1)
LF300	30(3)	28(1)	3(1)	0	3.7(1)	3.4(1)
LF500	5(1)	3(1)	1.5(5)	0	3.7(1)	3.6(1)

Tabelle 4.1: Characteristic values in the magnetization curves for the three (Li_2Fe)SO samples at 1.8 K and at 300 K.

as can be seen in Figure 4.10. The size of these secondary clusters grows with the temperature of the treatment[27]. It is expected that the samples contain impurities which are[27] ferromagnetic or (depending on the particle size) superparamagnetic elementary iron Fe[28] and magnetite Fe_3O_4[28], antiferromagnetic $LiFeO_2$[29] and FeS, which transitions from a high T AFM state to a magnetized (probably canted antiferromagnetic) phase at ≈ 70 K[30]. Elementary sulfur S may also be contained in the LFRT sample[27], this is simply diamagnetic and thus not expected to cause a large contribution to the sample's magnetic properties. It is necessary to understand both the magnetic properties of (Li_2Fe)So itself as well as the composition of the powders after the annealing process. Estimates on the amounts of the possible impurities present might be deducted from the magnetization data.

Due to air-sensitivity (oxidation) it was necessary to limit the exposure of the material to air as much as possible. This was achieved by storing all samples in an Argon filled glovebox. They were taken out of the Ar atmosphere wrapped in parafilm only shortly before installment into the MPMS. The measurement chamber of the MPMS is filled with He during the measurements so contact with air becomes negligible after installing.

The measurement consisted of isothermal and field-constant DC magnetization measurements at the MPMS3. They were performed in the same order for all three samples to increase comparability and are illustrated in Figure 4.12:

1. After centering, a $M(B)$ measurement was performed at 300 K in 300 Oe increments (50 Oe/s). 1a-c
2. The sample is cooled to 10 K (with 10 K/min) at zero field (ZFC).
3. A $M(B)$ measurement is performed at 1.8 K with the same parameters as before. 2a-c
4. After oscillating out the field, a $M(T)$ measurement is performed with reapplied 1 T. The temperature T is twice brought up to 350 K (ZFC and field cooled FC), the cooling with field is recorded as well (2 K/min, 175 stable temperatures spaced evenly in $T^{1/2}$). These are marked in Figure 4.12 as ZFC warming, FC cooling and FC warming.

Data from the isothermal field dependent magnetization measurements $M(B)$ at

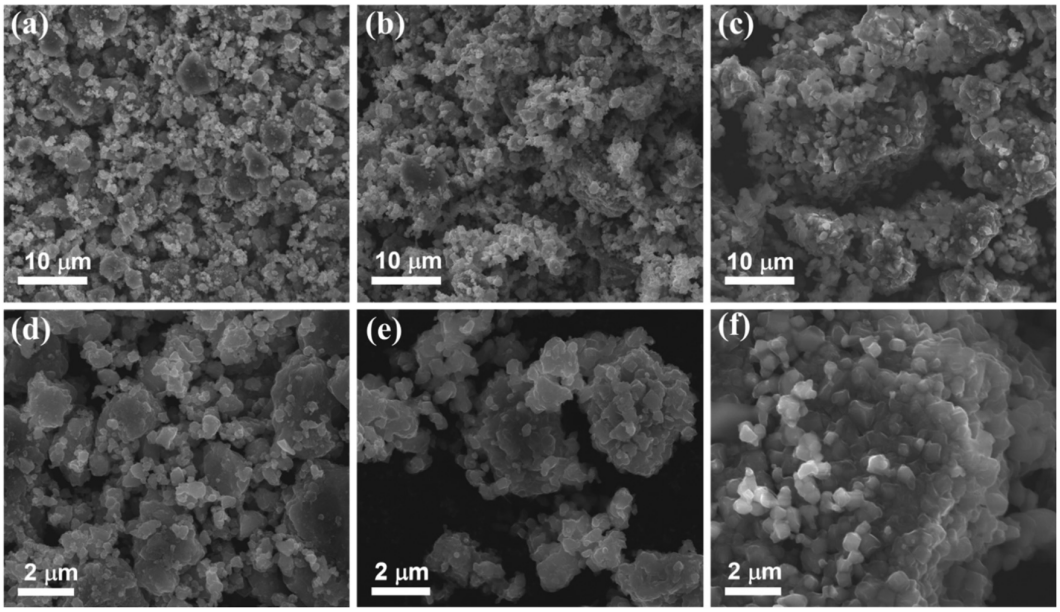


Abbildung 4.10: SEM images of (Li_2Fe)SO powder samples synthesized by the same process as the present ones: (a)&(d) were ball-milled and not heat-treated (similar to LFRT) (b)&(e) were additionally heat-treated at 300° C afterwards (similar to LF300), (c)&(f) were heat-treated at 500° C (similar to LF500) (picture taken from [27]).

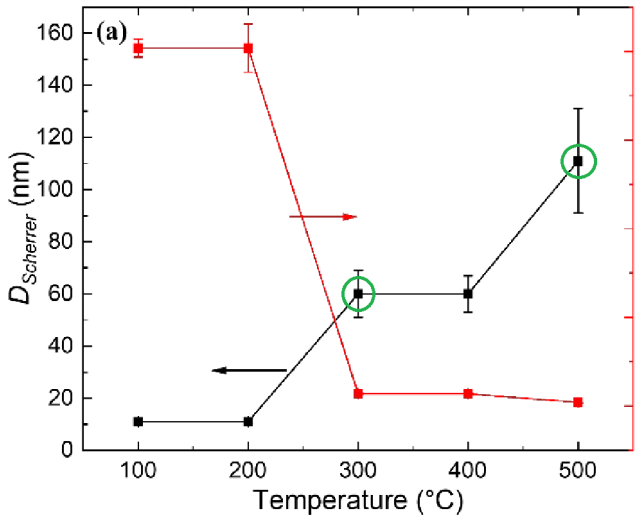


Abbildung 4.11: The sizes of crystallites in ball milled (Li_2Fe)SO as a function of annealing temperature. Green markers indicate the temperatures which are being further investigated here. The red line is not relevant here (taken and adapted from supplementary material of [27]).

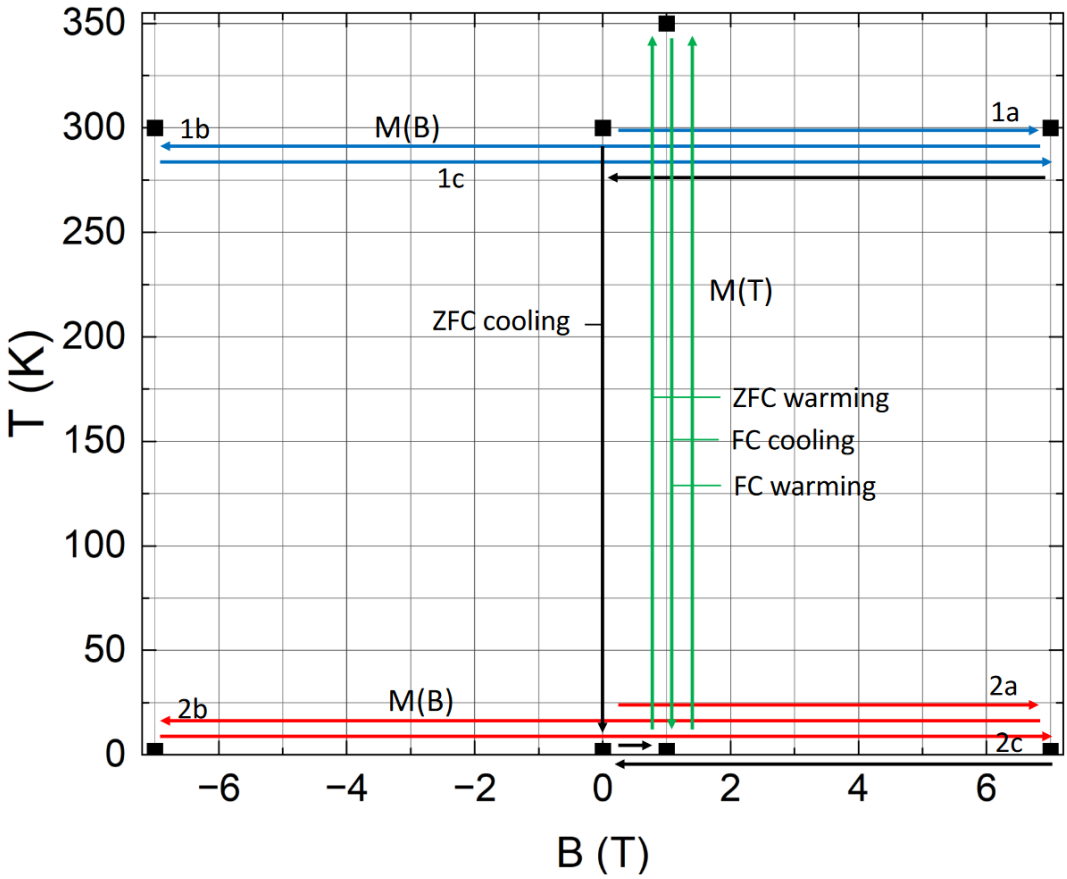


Abbildung 4.12: Measurement routine for $(Li_2Fe)SO$ samples in the B-T plane: The magnetization M is measured as a function of field B and temperature T. 1a-c and 2a-c are isothermal measurements at 300 K and 1.8 K respectively with a magnetic field between -7 T and 7 T along the c axis. The ZFC warming, FC cooling and FC warming sequences measure M against T at 1 T. M is not recorded during the state changes which are represented by black arrows.

1.8 K and 350 K are depicted in Figure 4.14 and Figure 4.15 respectively. Both datasets show a similar behavior: The magnetization data for LFRT starts with a steep increase in magnetization from 0 and saturates at $B_{\mathrm{sat}} \approx 1$ T, the saturation if followed by a slower constant increase in $M(B)$. After reversal of the field direction a remanent magnetization is observed. LF300 and LF500 show a significantly reduced magnetization, in particular are their M_{sat} reduced, M_{r} is only detected in the 1.8 K data. The gradient for high fields $|B| \gtrsim 1$ T is lower in the thermally treated samples (LF300/500) than in LFRT at 1.8 K but similar at 300 K. Table 4.1 lists the values for M_{sat}, M_{r} and χ_{PM} of the three samples.

Figure 4.16, Figure 4.17 and Figure 4.18 depict the temperature dependent static magnetic susceptibility $\chi(T) = M(T)/H$ and its temperature derivative $\partial\chi/\partial T$ of the three samples between 1.8 K and 350 K with an applied magnetic field of $B = 1$ T. The data for LFRT show a small initial decrease in magnetization below 4 K, followed by an increase into a broader maximum at $T_{\mathrm{max}} \approx 50$ K with $\chi_{\mathrm{max}} = 4.4 \times 10^{-2}$ erg/G^2/mol. χ drops afterwards, first steeply up to $T_{\mathrm{drop}} \approx 75$ K, then in a linear manner to $T_{\mathrm{A}} = 320$ K. For temperatures above T_{A} a significant drop in the susceptibility of $\Delta\chi^{(1)} \approx 2 \times 10^{-3}$ erg/G^2/mol is observed. In the following down sweep the drop continues for a further $\Delta\chi^{(2)} \approx 0.7 \times 10^{-3}$ erg/G^2/mol as long as $T \gtrsim 320$ K. The data then shows a behavior similar to the first warming down to 40 K. Below this no clear maximum in χ is visible as the susceptibility increases down to the lowest measured temperatures but the drop between $T = 75$ K and 50 K can still be seen. The last warming sweep resembles the preceding cooling process up to 320 K where a further drop in magnetization is seen, similar but slightly less pronounced than the first warming sweep with $\Delta\chi^{(3)} \approx 0.75 \times 10^{-3}$ erg/G^2/mol. Since the With the thermally treated samples LF300 and LF500 the described maximum at $T_{\mathrm{max}} = 50$ K and subsequent drop at T_{drop} get progressively more pronounced. No significant difference between the samples is seen in the high temperature behavior above T_{drop}. The difference between ZFC warming and FC warming/cooling is likewise visible, FC warming and cooling show no deviations. Between T_{max} and T_{drop} a significant decrease in $\partial\chi/\partial T$ is visible in all samples and all sweeps. FC warming and FC cooling data from LFRT and LF300 both show small peaks in $\partial\chi/\partial T$ at 220 K (for the cooling) and 230 K for warming.

Results of the temperature dependent magnetization measurement for the not heat-treated sample LFRT are shown in Figure 4.16 in the form of the magnetic susceptibility $\chi = M/B$ (see eq. (2.4)), which is not identical to the susceptibility $\chi = \partial M/\partial B$ as before (and thus not directly comparable with non linear regimes in $M(B)$).

For the analysis of the $M(B)$ data it proves useful to isolate the magnetization behavior of the seemingly saturated high field regime for fields above 1 T. The constant magnetic susceptibility in the high field regime can be interpreted as a paramagnetic contribution to the total susceptibility. Assuming that the Fe content in the (Li_2Fe)SO crystal is not significantly influenced by heat treatment, its Pauli paramagnetism could be one explanation for the observed behavior. It was described[19]

that the Fe^{2+} ions are the cause of the paramagnetism in $(Li_2Fe)SO$, this may then be an explanation for the (treatment temperature) constant susceptibility. The high field susceptibility in the LFRT sample at 1.8 K is significantly increased relative to all other measurements. An explanation for this is possibly an impurity which follows a Curie Weiss behavior (eq. (2.10)) down to low temperatures and whose (para)magnetism is thus increased at lower temperatures. To make this approach compatible to the observations of the LF300 and LF500 samples, this unknown impurity would need to vanish with heat treatment and therefore be converted below 300°C. The problem with this explanation is that no such compound was detected during XRD analysis[27].

Similar investigation were previously performed by Singer *et al.* on the sister anti-perovskite compound $(Li_2Fe)SeO$[31]. The samples were also fabricated through ball milling. Their data showed a saturation magnetization and a paramagnetic contribution as well. Differences between heat treated and not treated samples are reported but the trend is opposite: The treated sample (at 600°C) has a $60\% - 100\%$ higher saturation and paramagnetic component than the sample which was only ball milled. The influence of heat treatment in $(Li_2Fe)SeO$ is smaller than in $(Li_2Fe)SO$. This shows that the presently investigated $(Li_2Fe)SO$ sample has most likely a higher ferromagnetic contribution in Fe or Fe_3O_4 which probably stems from the specifics of the ball milling of this material. This then vanishes after being heat treated. A comparison between the two datasets is plotted in Figure 4.13.

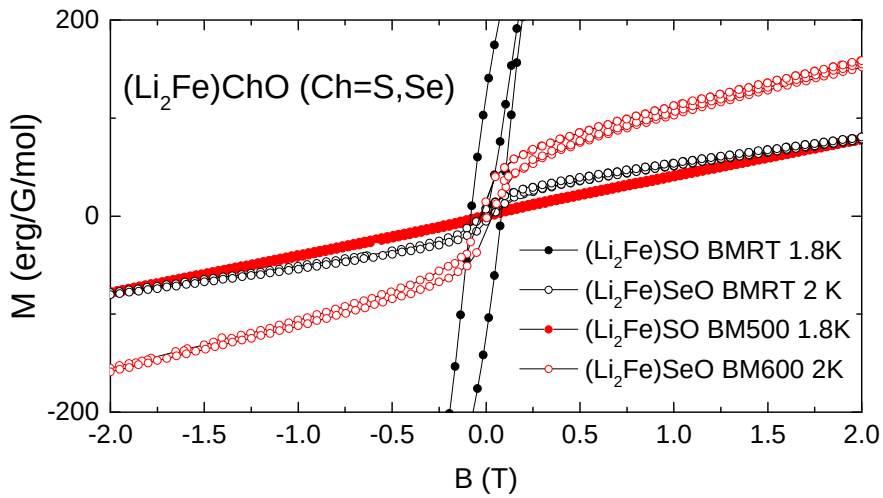


Abbildung 4.13: Comparing isothermal magnetization between $(Li_2Fe)SO$ and $(Li_2Fe)SeO$ (Data of the latter material from [31]).

To facilitate the analysis of the temperature dependent magnetization $M(T)$, it makes sense to correct the ZFC warming data for the offset caused by the drop above T_{drop}. This is achieved by shifting the data down by $\Delta\chi = \Delta\chi^{(1)} + \Delta\chi^{(2)} \approx 2.7 \times 10^{-3}$ erg/G^2/mol, as done in Figure 4.16 in white. A small discrepancy between the ZFC and FC curves is visible. This may be due to the behavior for $T > 320$ K. It has to be assumed that this indicates an irreversible degradation of (at least one) of the components of the powder at low temperature (320 K $\approx$ 50°C). Since the reduction in M (or χ) above 320 K is significant ($10\% - 15\%$) but independent of the measurement temperature and the paramagnetic component to the field dependent magnetization at higher fields χ_{PM} is mostly independent of the temperature (see Table 4.1), it can be assumed that this is caused by a decomposition of a Pauli paramagnetic compound.

The large ferromagnetic contribution in $M(B)$ especially in LFRT hints to either elementary Fe or Fe_3O_4, which both exhibit ferromagnetic behavior in bulk. Superparamagnetism has been observed for magnetite at 300 K with particle sizes of $\lesssim 20$ nm[32], particle sizes for elementary iron are even smaller[33]. Iron in the individual samples has been detected by XRD measurements[27] only in the samples which were heated up to 200°C; no pure iron was detected anymore after treatment at higher temperatures. The explanation for this was given as a possible solid state reaction of the iron with other material into $FeS/LiFeO_2$ which have a significantly lower magnetization[30]. This can explain the large hysteresis of the LFRT sample and its disappearance in the other two heat treated samples.

The temperature dependent magnetization data (Figure 4.16-Figure 4.18) all show a broad maximum at $T_{\mathrm{max}} \approx 50$ K for the ZFC warming sweeps, this is probably due to the fact that during the ZFC cooling the magnetic moments freeze in a random ordering which lowers the total magnetization[9]. When the temperature is raised with an applied field, the system will eventually have enough thermal energy to orient them along the field, this is visible here at T_{max}. If a magnetic field is applied during the cooling process (FC) this is not the case since the spins will freeze in an ordered state. Due to this the maximum is only visible in the ZFC data.

Another feature, which is not to be confused with the previously mentioned maximum, is the drop in magnetization visible between T_{max} and T_{drop}. One possible explanation for this feature could be that this is a Verwey transition, a transition between cubic and monoclinic order which is observed at $T_{\mathrm{V}} \approx 120$ K in Fe_3O_4[34]. An explanation for the shifted temperature can be that is is reportedly lowered in the case of non-stoichiometric $Fe_{3(1-\delta)}O_4$[34,35]. Extrapolating the data from [34] and assuming a Verwey transition temperature of $T_{\mathrm{V}} = 40$ K would lead to an iron deficiency of $\delta = 0.03(1)$ and thus $Fe_{2.91(3)}O_4$. The reports on the non-stoichiometric data however only report vales for δ up to 0.015. Thus extrapolating the data further down might overlook a non linear behavior in $T_{\mathrm{V}}(\delta)$ which is already reported at lower δ[34]. Verwey transitions are furthermore normally characterized by a rather sharp drop in magnetization which happens within a few K even for small grain

sizes[36], this is not observed here. Thus it is unlikely that the behavior at 40 K can be explained as a Verwey transition and that significant amounts of Fe_3O_4 present in the sample.

A similar kink at 50 K is also found in stoichiometric FeS[30]. The material transitions from a ferromagnetic to a high temperature antiferromagnetic phase in the same temperature range which coincides with the here reported data. This transition could explain the drop in susceptibility of the samples. Since [30] does not show consistent values for the relative size of the feature at 70 K, it is not possible to estimate the amount of FeS contained.

The peaks at 220/230 K show a thermal hysteresis in the sense that a heating sweep across this phenomenon leads to a higher detection temperature than a cooling sweep. An explanation could be a first order phase transition. This assumption is congruent with the observed hysteresis: The system tries to remain in the previous phase for some Kelvin. Since this vanishes for LF500, which has been annealed at the highest temperature, it can be argued that this is caused by a material that is converted between 300°C and 500°C. Looking at the XRD data[27], non-stoichiometric $FeS_{(1-x)}$ could be a candidate as it disappears from the spectrum above 400°C. Indeed it is reported[37] that $Fe_{0.95}S$ has an α transition between two antiferromagnetic phases at approximately 220 K. The amount of contained $Fe_{0.95}S$ can be estimated form the size of the phase transition: Comparing the jumps in the susceptibility $\Delta\chi_{\mathrm{LFRT}} = 7(1) \times 10^{-3}$ erg/G^2/mol and $\Delta\chi_{\mathrm{LFR300}} = 1.5(5) \times 10^{-3}$ erg/G^2/mol with the value for pure $Fe_{0.95}S$ $\Delta\chi = 1.0(5) \times 10^{-3}$ erg/G^2/mol yields contents of $A^{\mathrm{Fe_{0.95}S}} = 7.0\%_{\mathrm{mol}}$ in LFRT and $A^{\mathrm{Fe_{0.95}S}} = 1.5\%_{\mathrm{mol}}$ in LF300.

To get an estimate on the Fe/Fe_3O_4 content in LFRT, the characteristic values of its $M(B)$ behavior in Table 4.1 can be used. Since the magnetization from different species in the powder add up, the saturation and remanence will be used. First it will be assumed that the FM or SPM content in LFRT is predominantly caused by iron. Its saturation magnetization is (mostly grain size independent) $M_{\mathrm{sat}}^{\mathrm{Fe}} \approx 12300$ erg/G/mol[28]. Comparing this to the measured saturation in LFRT results in a percentage of $A^{\mathrm{Fe}} = 3.0(2)\%_{\mathrm{mol}}$. This is the upper bound of iron content in the sample. The same can be done for assuming a saturation which is caused purely by Fe_3O_4 with $M_{\mathrm{sat}}^{\mathrm{Fe}} \approx 22000$ erg/G/mol[28] and leads to a maximum $A^{\mathrm{Fe_3O_4}} = 1.7(1)\%_{\mathrm{mol}}$. In the LFRT sample these two materials are the only possible sources of ferromagnetism, since FeS has not been reported without heating the sample. The quotient of $M_{\mathrm{r}}/M_{\mathrm{sat}}$ for both Fe and Fe_3O_4 in bulk is smaller ($17-30\%$) than what is observed for the powder samples: For Fe it is reported to be $\approx 1/2$[28], for Fe_3O_4 it is $\approx 1/3$[38]. A contribution by superparamagnetic particles could explain this lower observed value. The same can be already said for particles with sizes below 1 μm[38] which are known to exist in the LFRT sample (see Figure 4.10 and [27]). Coming back to the previously mentioned discussion on Fe_3O_4 and the conclusion that it is likely not contained in the powder in larger quantities, it can be assumed that the ferromagnetic contribution is iron with a percentage of $A^{\mathrm{Fe}} \approx 3\%_{\mathrm{mol}}$. A problem

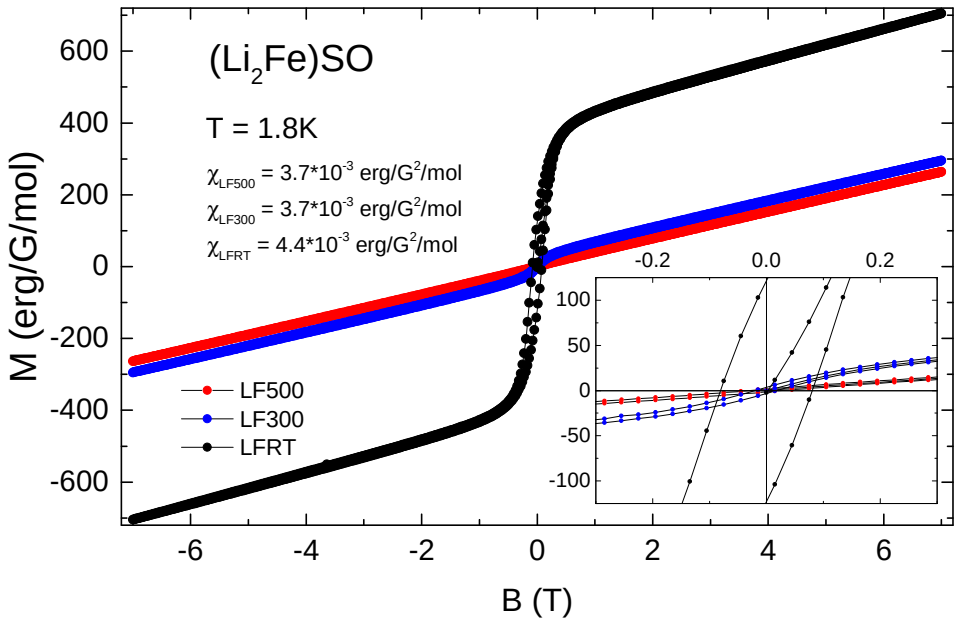


Abbildung 4.14: Results of isothermal magnetization measurements $M(B)$ on (Li$_2$Fe)SO samples at 1.8 K. The inset is zoomed in on the magnetization at low field strengths. χ_{LFx} describes the paramagnetic contribution to the total susceptibility.

with explaining the large magnetization through iron is the drop of susceptibility above 320 K since iron is stable in temperature. The decrease in M of up to 15% would correspond to losing the same share of iron which seems unlikely due to its thermal stability.

Because the saturation and remanence magnetizations of the annealed samples are so low (on the order of 10^1 erg/G/mol, it is not possible to give a reliable estimate on the content of either of the two possible ferromagnetic species in them. An estimate on the $LiFeO_2$ content cannot be made based on the magnetization data alone.

The magnetic investigations on the three (Li$_2$Fe)SO samples have supported the assumption that ca. 3%$_{\mathrm{mol}}$ of elementary iron are contained in the not heat treated samples, the other samples contain significantly less iron. This conclusion is possibly contradicted by a decrease in magnetization above 320 K which could not be attributed to iron. It is unlikely that the observed ferromagnetic behavior is due to Fe_3O_4. A phase transition was found at 220 K, which may show the presence of $Fe_{0.95}S$ in LFRT and LF300 with percentages of 7%$_{\mathrm{mol}}$ and 1.5%$_{\mathrm{mol}}$ respectively.

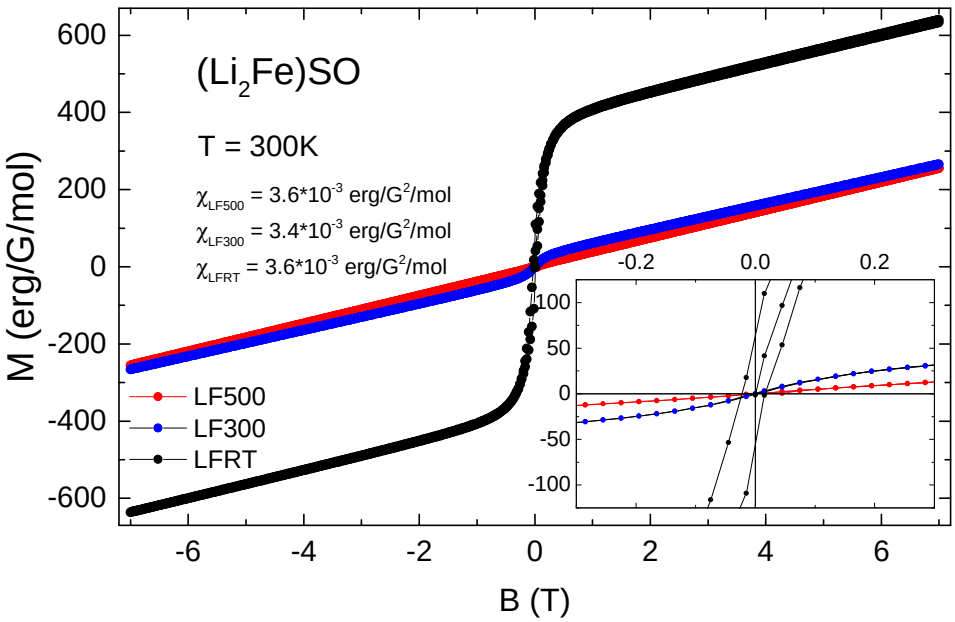


Abbildung 4.15: Results of isothermal magnetization measurements $M(B)$ on $(Li_2Fe)SO$ samples at 300 K. The inset is zoomed in on the magnetization at low field strengths. χ_{LFx} describes the paramagnetic contribution to the total susceptibility.

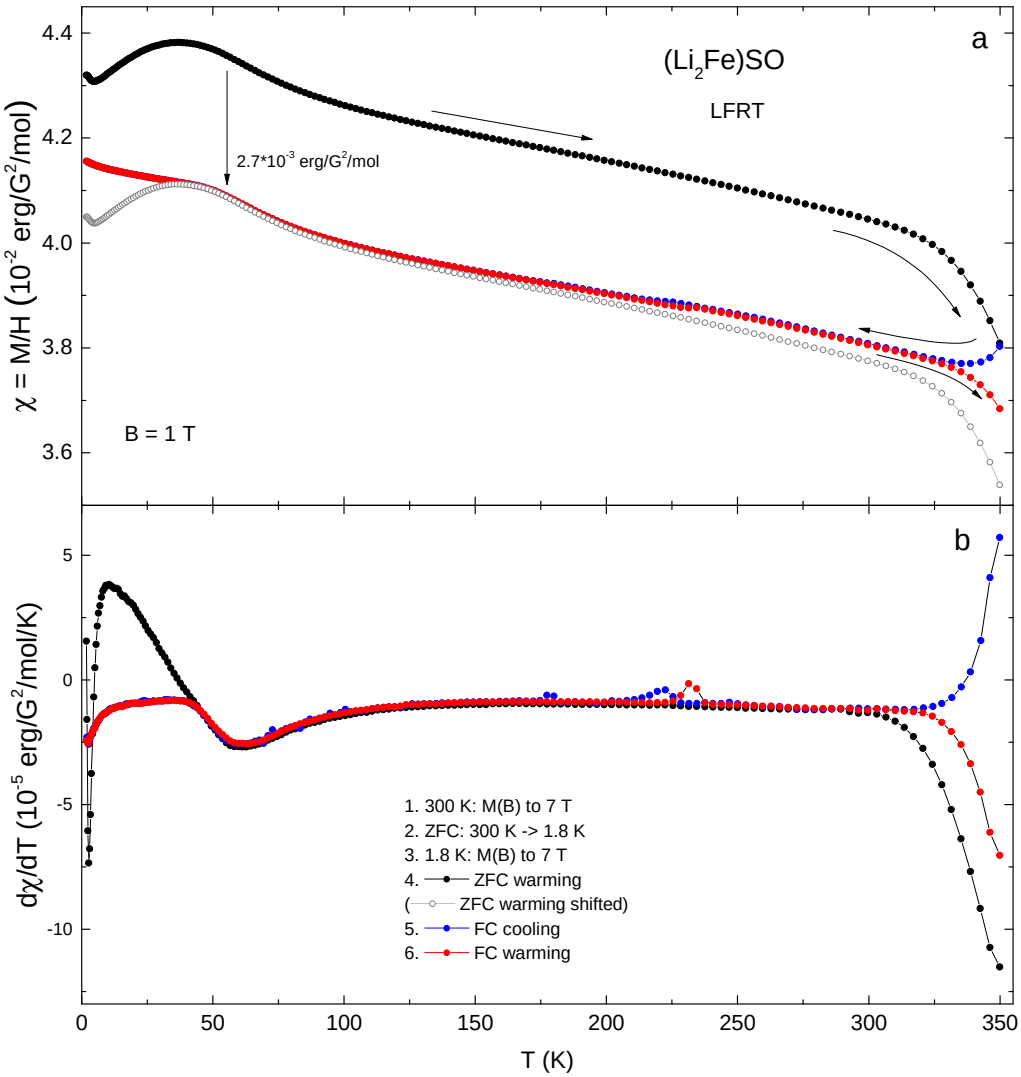


Abbildung 4.16: Temperature dependent magnetic susceptibility $\chi(T) = M(T)/H$ of the not heat-treated $(Li_2Fe)SO$ sample LFRT with an applied magnetic field $B = 1$ T. Arrows mark the direction of measurement. The white dots do not mark a separate measurement but only the shifted ZFC warming data (in black).

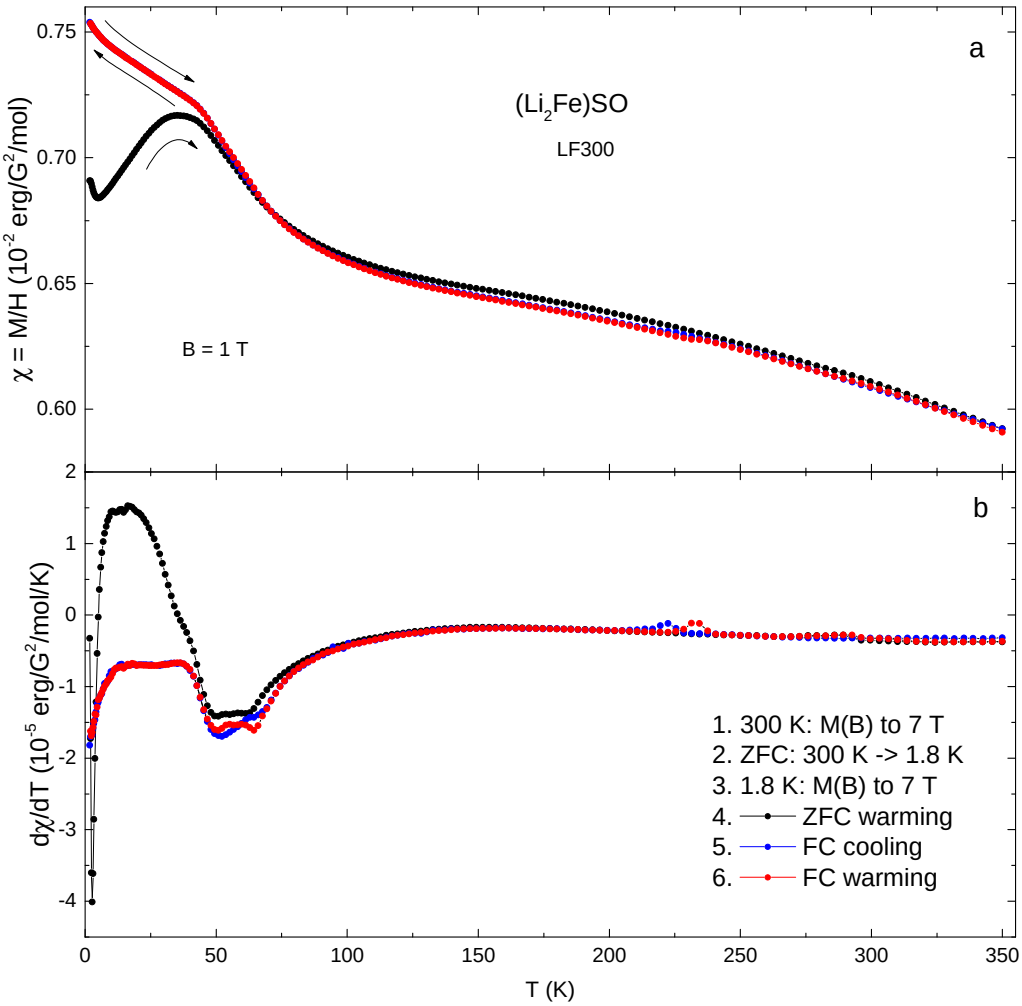


Abbildung 4.17: Temperature dependent magnetic susceptibility $\chi(T) = M(T)/H$ of the 300°C heat-treated (Li_2Fe)SO sample LF300 with an applied magnetic field $B = 1$ T. Arrows mark the direction of measurement.

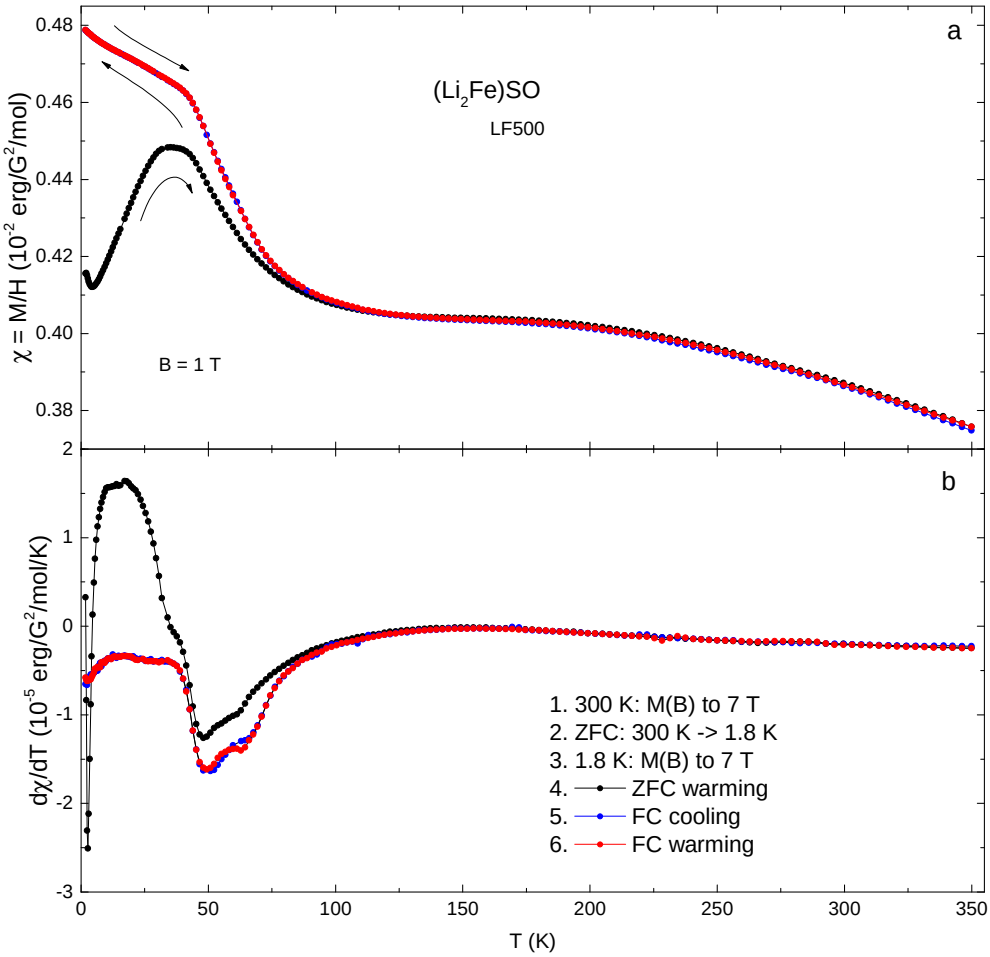


Abbildung 4.18: Temperature dependent magnetic susceptibility $\chi(T) = M(T)/H$ of the 500°C heat-treated (Li_2Fe)SO sample LF500 with an applied magnetic field $B = 1$ T. Arrows mark the direction of measurement.

Kapitel 5

Conclusion and summary

In the course of this work three different materials were investigated regarding their DC magnetic properties: In NdB_4 the isothermal field dependent magnetization was studied at temperatures between 9 K and 17.5 K for fields up to 14 T along its c axis. The results are compared to previous data obtained at lower temperatures. Measurements on a thin film of $MnTeMoO_6$ were performed to study its isothermal magnetization between 1.8 K and 17 K and fields up to 7 T along the c axis (perpendicular to the film) and its temperature dependent magnetization between 1.8 K and 350 K at a field of 0.1 T. Lastly, three samples of $(Li_2Fe)SO$ powder were investigated for isothermal magnetization at 300 K and 1.8 K with fields up to 7 T and for its temperature dependent magnetization at temperatures from 1.8 K to 350 K at 1 T.

The isothermal field dependent magnetization measurements for NdB_4 for fields applied along the c axis show a saturation into a plateau at all investigated temperatures similar to previous works. This plateau can be interpreted as having a magnetization equal to half the theoretically calculated saturation magnetization of the Nd^{3+} moments. An explanation for this plateau was proposed as being based on additional ferro and antiferromagnetic interactions between the magnetic moments which is supported by previous numerical simulations. The transition from a linear behavior into the saturated plateau is marked by two temperature dependent critical fields. To confirm the hypothesis of a half saturated plateau it would be necessary to measure the magnetization behavior at higher fields. These findings were incorporated into magnetic phase diagram.

Measurements on the thin film sample of $MnTeMoO_6$ did not provide any meaningful results. Because of the small amount of sample available, the signal was too weak and thus not detectable against the background.

The observed magnetic properties of the three $(Li_2Fe)SO$ samples differ significantly. In the pristine sample, a large ferromagnetic impurity phase is observed. It is suggested to be elementary iron in the amount of approximately 3% based on the saturation magnetization. To explain the remanence which is lower than expected for bulk iron, it was necessary to assume a significant part of the iron to be in the form of superparamagnetic particles. Arguments were brought forth as to why Fe_3O_4 is not a probable explanation for this. A thermal instability of parts of the not heat treated powder in the pristine sample resulting on a loss of approximately

15% of the magnetization was observed above 320 K. This can be understood as an argument against the hypothesis of elementary iron impurities in the sample. Higher treatment temperatures lead to a significant decrease in the ferromagnetic properties of the samples which is in agreement with previous investigations on the Fe content. This is explained through the conversion of iron into other less magnetic species at elevated temperatures during the annealing. Features in the temperature dependent magnetization can be interpreted as evidence for the presence of $Fe_{(1-x)}S$ with $x \approx 0.05$ at 1.5% in LK300 and 7% in LFRT.

Literatur

[1] Aristoteles, *De anima*, eng, hrsg. von C. Shields, First edition, Clarendon Aristotle Series, Translated from the Ancient Greek. (Clarendon Press, Oxford, 2016).

[2] B. Cullity und C. Graham, *Introduction to Magnetic Materials* (Wiley, 2011).

[3] R. Goldfarb und F. Fickett, „UNITS FOR MAGNETIC PROPERTIES“, NBS Special Publication 696 (1985).

[4] S. Hunklinger und C. Enss, *Solid state physics* (De Gruyter, Berlin ; Boston, 2022).

[5] R. Gross und A. Marx, *Festkörperphysik*, 4., aktualisierte Auflage, De Gruyter Studium (De Gruyter, Berlin ; Boston, 2023).

[6] S. Blundell, *Magnetism in Condensed Matter*, Oxford master series in condensed matter physics (Oxford University Press, 2001).

[7] H. Föll und J.-M. Wagner, *Grundlagen der Materialwissenschaft für Elektro- und Informationstechniker*, German, Version 17/02/2022, Christian-Albrechts-Universität Kiel, Technische Fakultät, (2008) https://www.tf.uni-kiel.de/matwis/amat/mw_for_et/index.html.

[8] T.-H. Chang, „Ferrite Materials and Applications“, in *Electromagnetic Materials and Devices*, hrsg. von M.-G. Han (IntechOpen, Rijeka, 2019) Kap. 7.

[9] S. Mugiraneza und A. Hallas, „Tutorial: a beginner's guide to interpreting magnetic susceptibility data with the Curie-Weiss law“, Commun Phys **5**, https://doi.org/10.1038/s42005-022-00853-y (2022).

[10] D. Brunt, M. Ciomaga Hatnean, O. A. Petrenko, M. R. Lees und G. Balakrishnan, „Single-Crystal Growth of Metallic Rare-Earth Tetraborides by the Floating-Zone Technique“, Crystals **9**, 10.3390/cryst9040211 (2019).

[11] R. Ohlendorf, *Thermische Ausdehnung und Magnetostriktion von NdB_4*, Bachelor's thesis, 2021.

[12] R. Ohlendorf, S. Spachmann, L. Fischer, K. Dey, D. Brunt, G. Balakrishnan, O. A. Petrenko und R. Klingeler, „Magnetoelastic coupling and Grüneisen scaling in NdB_4“, Phys. Rev. B **103**, 104424 (2021).

[13] R. Ohlendorf, S. Spachmann, L. Fischer, R. Klingeler, D. Brunt, G. Balakrishnan und O. Petrenko, „Magnetic phase diagram of NdB_4 studied by high-resolution capacitance dilatometry up to 35 T“, To be published.

[14] N. Metoki, H. Yamauchi, M. Matsuda, J. A. Fernandez-Baca, R. Watanuki und M. Hagihala, „Polarized neutron scattering study of the multiple order parameter system NdB_4“, Phys. Rev. B **97**, 174416 (2018).

[15] R. Watanuki, T. Kobayashi, R. Noguchi und K. Suzuki, „Possible multipolar transition in NdB 4“, Journal of Physics: Conference Series **150**, 042229 (2009).

[16]C. Jin, M. Wan, L. Huang, J. Shao und F. Wang, „Experimental and theoretical studies of optical and nonlinear optical properties for MnTeMoO6 crystal“, Journal of Alloys and Compounds **651**, 585–589 (2015).
[17]Y. Doi, R. Suzuki, Y. Hinatsu und K. Ohoyama, „Magnetic and neutron diffraction study on quaternary oxides MTeMoO6 (M= Mn and Zn)“, Journal of Physics: Condensed Matter **21**, 046006 (2009).
[18]C. Jin und L. Liu, „Experimental and theoretical studies of magnetic properties for $MnTeMoO_6$ crystal“, Journal of Alloys and Compounds **747**, 591–594 (2018).
[19]D. Mikhailova, L. Giebeler, S. Maletti, S. Oswald, A. Sarapulova, S. Indris, Z. Hu, J. Bednarcik und M. Valldor, „Operando Studies of Antiperovskite Lithium Battery Cathode Material (Li2Fe)SO“, ACS Applied Energy Materials **1**, 6593–6599 (2018).
[20]Z. Lu und F. Ciucci, „Anti-perovskite cathodes for lithium batteries“, J. Mater. Chem. A **6**, 5185–5192 (2018).
[21]E. Walendy, „Untersuchungen der magnetischen Eigenschaften des Van-der-Waals-Materials CrI_3“, Bachelor's thesis (KIP, Heidelberg University, 2020).
[22]Q. Design, *Magnetic Property Measurement System, MPMS 3 User's Manual* (2016).
[23]Q. Design, *Physical Property Measurement System, Vibration Sample Magnetometer (VSM) Option User's Manual* (2008).
[24]M. J. Coak, C. Liu, D. M. Jarvis, S. Park, M. J. Cliffe und P. A. Goddard, „SquidLab—A user-friendly program for background subtraction and fitting of magnetization data“, Review of Scientific Instruments **91** (2020).
[25]D. Brunt, G. Balakrishnan, D. Mayoh, M. R. Lees, D. Gorbunov, N. Qureshi und O. Petrenko, „Magnetisation process in the rare earth tetraborides, NdB4 and HoB4“, Scientific Reports **8**, 232 (2018).
[26]L. Huo, W. C. Huang, Z. B. Yan, X. T. Jia, X. S. Gao, M. H. Qin und J.-M. Liu, „The competing spin orders and fractional magnetization plateaus of the classical Heisenberg model on Shastry-Sutherland lattice: Consequence of long-range interactions“, Journal of Applied Physics **113**, 073908 (2013).
[27]M. A. A. Mohamed, H. A. A. Saadallah, I. G. Gonzalez-Martinez, M. Hantusch, M. Valldor, B. Büchner, S. Hampel und N. Gräßler, „Mechanochemical synthesis of Li-rich (Li2Fe)SO cathode for Li-ion batteries“, Green Chem. **25**, 3878–3887 (2023).
[28]R. M. Bozorth, *Ferromagnetism*, eng, An IEEE Press classic reissue, Literaturverz. S. 875 - 946 (IEEE Press, Piscataway, NJ, 1993), XVII, 968 S.
[29]E. Chappel, M. Holzapfel, G. Chouteau und A. Ott, „Effect of Cobalt on the Magnetic Properties of the LiFe1xCoxO2 Layered System (0x1)“, Journal of Solid State Chemistry **154**, 451–459 (2000).
[30]J. Cuda, T. Kohout, J. Tucek, J. Haloda, J. Filip, R. Prucek und R. Zboril, „Low-temperature magnetic transition in troilite: A simple marker for highly stoichiometric FeS systems“, Journal of Geophysical Research: Solid Earth **116**, https://doi.org/10.1029/2011JB008232 (2011).

[31]L. Singer, M. Mohamed, H. Hahn, I. G. Gonzalez-Martinez, M. Hantusch, K. Wenelska, E. Mijowska, B. Büchner, S. Hampel, N. Gräßler u. a., „Elucidating the electrochemical reaction mechanism of lithium-rich antiperovskite cathodes for lithium-ion batteries as exemplified by (Li 2 Fe) SeO.“, Journal of Materials Chemistry A (2023).

[32]J. Baumgartner, L. Bertinetti, M. Widdrat, A. M. Hirt und D. Faivre, „Formation of magnetite nanoparticles at low temperature: from superparamagnetic to stable single domain particles“, PloS one **8**, e57070 (2013).

[33]M. Alagiri, C. Muthamizhchelvan und S. Ponnusamy, „Structural and magnetic properties of iron, cobalt and nickel nanoparticles“, Synthetic metals **161**, 1776–1780 (2011).

[34]Z. Kakol, „Magnetic and transport properties of magnetite in the vicinity of the Verwey transition“, Journal of Solid State Chemistry **88**, 104–114 (1990).

[35]R. Aragón, D. J. Buttrey, J. P. Shepherd und J. M. Honig, „Influence of nonstoichiometry on the Verwey transition“, Phys. Rev. B **31**, 430–436 (1985).

[36]A. V. Smirnov, „Grain size dependence of low-temperature remanent magnetization in natural and synthetic magnetite: Experimental study“, Earth, planets and space **61**, 119–124 (2009).

[37]K. Adachi und S. Ogawa, *1.1.3.1.5 Fe(1-x)X (X = S, Se, Te): Datasheet from Landolt-Börnstein - Group III Condensed Matter Volume 27A: Pnictides and Chalcogenides I in SpringerMaterials*, hrsg. von H. Wijn, Part of SpringerMaterials (Springer-Verlag Berlin Heidelberg).

[38]A. V. Smirnov und J. A. Tarduno, „Magnetic field control of the low-temperature magnetic properties of stoichiometric and cation-deficient magnetite“, Earth and Planetary Science Letters **194**, 359–368 (2002).

Eigenständigkeitserklärung

Ich versichere, dass ich diese Arbeit selbstständig verfasst und keine anderen als die angegebenen Quellen und Hilfsmittel benutzt habe.

Heidelberg, 31. Juli 2023
Frederik Leon Carstens

